

Chandra[★] X-ray observation of the young stellar cluster NGC 3293 in the Carina Nebula Complex^{★★}

T. Preibisch¹, S. Flaischlen¹, B. Gaczkowski¹, L. Townsley², and P. Broos²

¹ Universitäts-Sternwarte München, Ludwig-Maximilians-Universität, Scheinerstr. 1, 81679 München, Germany
e-mail: preibisch@usm.uni-muenchen.de

² Department of Astronomy & Astrophysics, Pennsylvania State University, University Park PA 16802, USA

Received March 27, 2017; accepted July 11, 2017

ABSTRACT

Context. NGC 3293 is a young stellar cluster at the northwestern periphery of the Carina Nebula Complex that has remained poorly explored until now.

Aims. We characterize the stellar population of NGC 3293 in order to evaluate key parameters of the cluster population such as the age and the mass function, and to test claims of an abnormal IMF and a deficit of $M \leq 2.5 M_{\odot}$ stars.

Methods. We performed a deep (70 ksec) X-ray observation of NGC 3293 with *Chandra* and detected 1026 individual X-ray point sources. These X-ray data directly probe the low-mass ($M \leq 2 M_{\odot}$) stellar population by means of the strong X-ray emission of young low-mass stars. We identify counterparts for 74% of the X-ray sources in our deep near-infrared images.

Results. Our data clearly show that NGC 3293 hosts a large population of \approx solar-mass stars, refuting claims of a lack of $M \leq 2.5 M_{\odot}$ stars. The analysis of the color magnitude diagram suggests an age of $\sim 8 - 10$ Myr for the low-mass population of the cluster. There are at least 511 X-ray detected stars with color magnitude positions that are consistent with young stellar members within 7 arcmin of the cluster center. The number ratio of X-ray detected stars in the $[1 - 2] M_{\odot}$ range versus the $M \geq 5 M_{\odot}$ stars (known from optical spectroscopy) is consistent with the expectation from a normal field initial mass function. Most of the early B-type stars and $\approx 20\%$ of the later B-type stars are detected as X-ray sources.

Conclusions. Our data shows that NGC 3293 is one of the most populous stellar clusters in the entire Carina Nebula Complex (very similar to Tr 16 and Tr 15; only Tr 14 is more populous). The cluster probably harbored several O-type stars, whose supernova explosions may have had an important impact on the early evolution of the Carina Nebula Complex.

Key words. Stars: formation – Stars: pre-main-sequence – X-ray: stars – open clusters and associations: NGC 3293

1. Introduction

The Carina Nebula Complex (CNC; see Smith & Brooks 2008, for a review) is one of the most massive and active star forming regions in our Galaxy. At a moderate and well-known distance of 2.3 kpc (Smith 2006), the spatial extent of the nebulosity of about 100 pc corresponds to several degrees on the sky. An optical image of the CNC is shown in Fig. 1. The clouds contain a total gas and dust mass of about $10^6 M_{\odot}$ (Preibisch et al. 2012) and harbor more than 100 000 young stars (Feigelson et al. 2011; Povich et al. 2011; Preibisch et al. 2011b; Zeidler et al. 2016). Most of these young stars are located in one of several clusters, including the extensively studied clusters Tr 14, 15, and 16 in the central regions of the Carina Nebula, and the clusters NGC 3324 and NGC 3293 in the northern part of the CNC.

Over the last years, several sensitive surveys of large parts of the CNC have been performed at optical and infrared wavelengths (e.g., Smith et al. 2010a,b; Preibisch et al. 2011c,b, 2012, 2014b). However, due to the location of the CNC very close to the Galactic plane, all optical and infrared images are com-

pletely dominated by unrelated field stars in the galactic background, which presents a major obstacle in the identification of the young stellar population in the complex. X-ray observations provide a very good way to solve this problem because strong X-ray emission is a very good tracer of stellar youth and allows very young stars to be efficiently distinguished from the numerous (and much older) field stars in the galactic background (see Feigelson et al. 2007). A major milestone in the exploration of the CNC was therefore the deep X-ray imaging survey of the *Chandra* Carina Complex Project (CCCP; see Townsley et al. 2011, for an overview), which mapped the central 1.4 square degrees (i.e., roughly half of the total spatial extent of the CNC) with a mosaic of 22 individual pointings with the Imaging Array of the *Chandra* Advanced CCD Imaging Spectrometer (ACIS-I; see Garmire et al. 2003). The *Chandra* data revealed 14 368 individual X-ray sources, 10 714 of which are most likely young stars in the Carina Nebula (Broos et al. 2011a) with masses down to $\sim 0.5 M_{\odot}$. The combination of these CCCP X-ray data with a deep near-infrared (NIR) survey (Preibisch et al. 2011b) provides information about the properties of the stellar populations in the central parts of the complex (Preibisch et al. 2011a), including the individual stellar clusters Tr 16 and Tr 15 (Wolk et al. 2011; Wang et al. 2011).

The northern parts of the cloud complex, including the young stellar clusters NGC 3324 and NGC 3293, were much less well explored because this area was not included in the CCCP and,

* The *Chandra* data described in this paper have been obtained in the open time project with ObsID 16648 (PI: T. Preibisch) [ivo://ADS/Sa.CXO#obs/16648](http://adsabs.harvard.edu/abs/2017arXiv1707.08782v1).

** Tables 1, 2, and 3 are only available in electronic form at the CDS via anonymous ftp to cdsweb.u-strasbg.fr (130.79.128.5) or via <http://cdsweb.u-strasbg.fr/cgi-bin/qcat?J/A+A/>

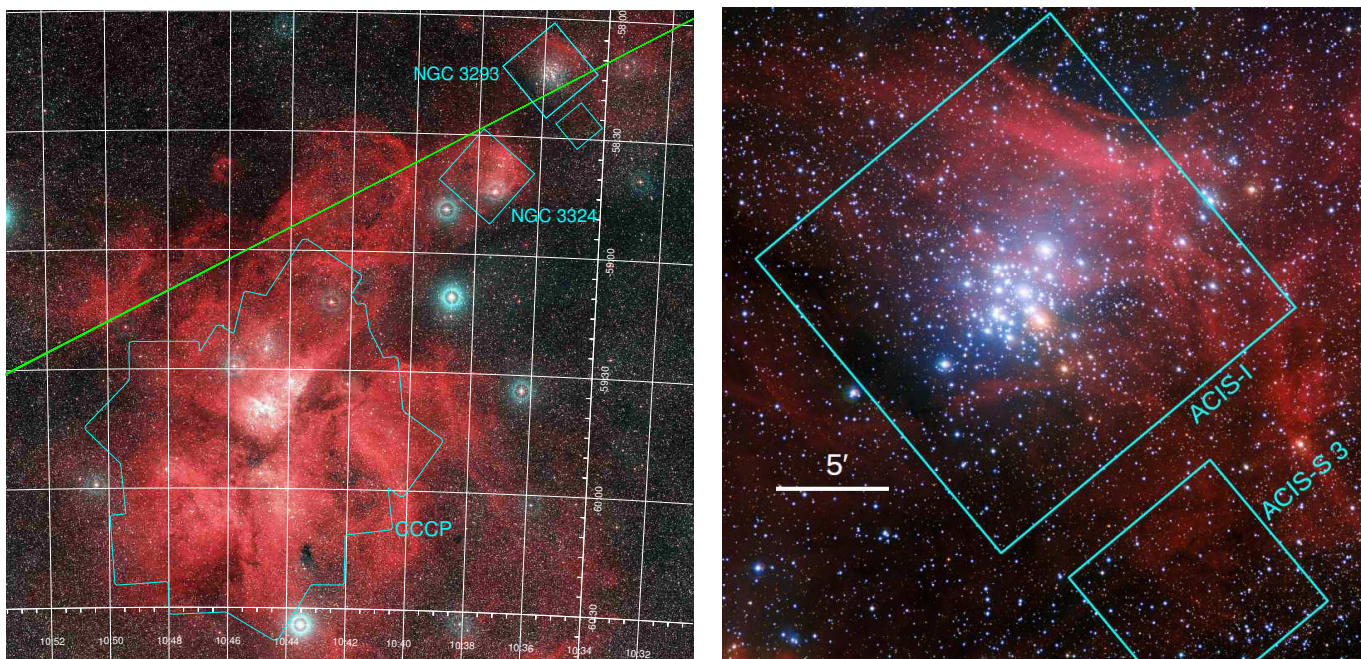


Fig. 1. Left: Optical image of the Carina Nebula Complex (from: www.eso.org/public/images/eso0905b/; image credit: ESO/Digitized Sky Survey 2, Davide De Martin). North is up and east to the left. The region observed in the context of the *Chandra* Carina Complex Project (CCCP) and the *Chandra* pointings of NGC 3324/Gum 31 and NGC 3293 are marked by the cyan outlines and labeled.

Right: Optical image of the cluster NGC 3293 (from: www.eso.org/public/images/eso1422a/; image credit: ESO/G. Beccari), composed from images taken with the MPG/ESO 2.2m telescope in the *B*-band (blue color channel), *V*-band (green color channel), *I*-band (orange color channel), and an *H α* filter (red color channel). North is up and east to the left. The central cyan rectangle marks the area covered by our *Chandra* observation with the ACIS-I array, the lower cyan rectangle (extending beyond the edge of the image) marks the area covered by the single active ACIS-S detector.

until recently, no deep infrared survey was available. The new very wide-field (6.7 square degrees) NIR survey with the ESO 4m VISTA telescope (see Preibisch et al. 2014b) finally solved this problem; these data are sensitive enough to detect the full stellar population of young stars down to $\sim 0.1 M_{\odot}$ over the entire area of the CNC, including the less studied northern parts.

As a first step in the X-ray exploration of the young stellar populations in these northern parts of the CNC (outside the field covered by the CCCP), we recently obtained a *Chandra* ACIS-I pointing of the stellar cluster NGC 3324 in the prominent HII region Gum 31 (Preibisch et al. 2014a), which led to the detection of 679 new X-ray sources.

The only cluster in the CNC that had not yet been observed in X-rays was NGC 3293 (also known as the “Gem Cluster”). Although this cluster is a very prominent celestial object (see Fig. 1), it was often neglected in studies of the CNC because of its angular separation of $\sim 1.5^{\circ}$ (70 pc) from the center of the Carina Nebula. Recent distance estimates for NGC 3293 (based on optical photometry) of ≈ 2327 pc (Dias et al. 2002) and ≈ 2471 pc (Kharchenko et al. 2005) are very consistent (within their uncertainties) with the distance of the Carina Nebula (2.3 kpc). The extinction for most stars in the cluster center is quite low ($A_V \lesssim 1$ mag), but increases up to several magnitudes for stars more than a few arcmin away from the cluster center, due to the interstellar clouds around the cluster (see Appendix A).

NGC 3293 contains an impressive collection of bright stars, including 48 early B-type stars (Evans et al. 2005) and several supergiants, e.g., HD 91969 (B0Ib) and V361 Car (M1.5Iab). The presence of evolved massive stars, main-sequence stars up to spectral type B0.5 V, and comparisons of optical color magnitude diagrams with stellar evolution models suggested an age

of $\approx 8 - 10$ Myr for the high-mass population in this cluster (Slawson et al. 2007; Delgado et al. 2011).

Another reason that makes NGC 3293 particularly interesting are claims for an abnormal stellar initial mass function (IMF) and an apparent severe lack of low-mass stars. In their analysis of optical photometry, Slawson et al. (2007) came to the conclusion that the cluster’s IMF shows a sharp turnover at masses below $2.4 M_{\odot}$. They argue that NGC 3293 is the cluster with the most convincing evidence for a strong deficit of low-mass stars. Delgado et al. (2011) also arrived at a similar conclusion from their optical photometry study, which suggested that the mass function is considerably flatter than the Salpeter slope below $2.5 M_{\odot}$.

These results, however, as well as all the other studies of the low-mass population of NGC 3293 performed so far, were only based on photometric observations. In the analysis of color magnitude diagrams of stellar clusters, the statistical background subtraction can introduce a very serious source of uncertainties, in particular at locations close to the galactic plane. Much more reliable information about the cluster properties and mass function can be obtained if the low-mass stellar members of the cluster can be individually identified.

The main obstacle for a reliable identification of the low-mass stellar population of NGC 3293 is the confusion by the very strong field star contamination resulting from the cluster’s location very close to the galactic plane: the cluster center has a galactic latitude of $b = +0.08^{\circ}$. All optical and infrared images are therefore strongly contaminated by unrelated field stars. The approach most often used to identify young stars is by the infrared excess emission from circumstellar disks, which is not feasible here. At an age of ~ 8 Myr, most stars should have already lost their circumstellar accretion disks and thus do not exhibit infrared excesses (e.g., Fedele et al. 2010). It is thus es-

entially impossible to identify and distinguish a population of $\sim 8 - 10$ Myr old low-mass stars from unrelated field stars with optical or infrared photometry alone.

Chandra, however, can solve this problem because the strongly enhanced X-ray emission of young stars (Feigelson et al. 2007; Preibisch et al. 2005) provides an extremely useful way to discriminate between young pre-main-sequence stars and the much older field stars. The median X-ray luminosity of ~ 10 Myr old solar-mass stars is nearly 1000 times higher than for solar-mass field stars (see Preibisch & Feigelson 2005), and makes these young stars relatively easy targets to detect for *Chandra* even at a distance of 2.3 kpc. A *Chandra* observation of NGC 3293 can uncover an X-ray luminosity-limited (i.e., approximately mass-limited) sample of the low-mass stellar population, provide a comprehensive census of the cluster members, and immediately answer the open questions about the size of the low-mass stellar population (and thus the total cluster mass).

2. *Chandra* X-ray observation and data analysis

We used the *Chandra* X-ray observatory (Weisskopf et al. 2002) to perform a deep pointing of the cluster NGC 3293 with the Imaging Array of the *Chandra* Advanced CCD Imaging Spectrometer (ACIS-I; see Garmire et al. 2003). The observation was performed as an open time project with ObsID 16648 (PI: T. Preibisch) during *Chandra* Observing Cycle 15 in October 2015 (start date: 2015-10-07T10:14:23, end date: 2015-10-08T06:43:28). The imaging array ACIS-I provides a field of view of $17' \times 17'$ on the sky (which corresponds to 11.3×11.3 pc at the distance of 2.3 kpc), and has a pixel size of $0.492''$. The point spread function of the X-ray telescope has a FWHM of $0.5''$ on-axis, but increases towards the edge of the detector. As part of our data analysis, the *Chandra* data were astrometrically registered to 2MASS to improve the absolute astrometry. The positions of bright X-ray sources can thus usually be determined with subarcsecond precision.

The observation was performed in the standard “Timed Event, Very Faint” mode with 5×5 pixel event islands, and the total effective exposure time (“livetime”) of the observation was 70 870 s (19.68 hours).

In addition to ACIS-I, one CCD detector (CCD 7 = S3) of the spectroscopic array ACIS-S was also operational during our pointing. It covers a $8.3' \times 8.3'$ area on the sky southwest of the cluster center. While the ACIS-I chips are front-illuminated, the S3 chip is back-illuminated, and thus its response extends to energies below that accessible by the FI chips. This causes a substantially higher level of background in the S3 chip. Furthermore, the point spread function is seriously degraded at the rather large off-axis angles of the S3 chip. These two effects lead to a considerably higher detection limit for point sources in the area covered by the S3 chip compared to the region covered by the ACIS-I array. Nevertheless, the S3 data were included in our data analysis and source detection, and contributed four point sources to the total source list.

The aimpoint of the observation was $\alpha(\text{J2000}) = 10^{\text{h}} 35^{\text{m}} 50.07^{\text{s}}$, $\delta(\text{J2000}) = -58^{\circ} 14' 00''$, which is close to the optical center of the cluster (see Fig. 1). The pointing roll angle (i.e., the orientation of the detector with respect to the celestial north direction) was 140.19° .

The resulting X-ray image is shown in Fig. 2. Clearly hundreds of X-ray sources are detected, with the greatest concentration at the cluster center. The gaps between the four ACIS-I CCDs are discernible as a light cross bisecting the image in two directions; the effective exposure time is reduced in these gaps.

Figure 3 shows a RGB color composite version of the *Chandra* image with color-coding corresponding to photon energy. X-ray sources can appear harder (bluer) because of their intrinsic spectral shape or because they suffer high absorption.

At the distance of 2.3 kpc, the expected ACIS point source sensitivity limit for a three-count detection on-axis in a 71 ks observation is $L_{\text{X,min}} \approx 10^{29.7}$ erg s^{-1} in the $[0.5 - 8]$ keV band, assuming an extinction of $A_V \approx 1$ mag ($N_{\text{H}} \approx 2 \times 10^{21}$ cm^{-2}) as typical for the stars in the central region of NGC 3293, and a thermal plasma with $kT = 1$ keV (which is a typical value for young stars; see, e.g., Preibisch et al. 2005). Using the empirical relation between X-ray luminosity and stellar mass and the temporal evolution of X-ray luminosity from the sample of young stars in the Orion Nebula Cluster, which was very well studied in the *Chandra* Orion Ultradeep Project (Preibisch et al. 2005; Preibisch & Feigelson 2005), we can expect to detect $\approx 90\%$ of the \approx solar-mass stars in the central region of the young cluster NGC 3293.

2.1. X-ray point-source detection and extraction with ACIS Extract

Source detection and analysis followed the steps described in Broos et al. (2010, 2012) (hereafter B10); we provide a brief summary of this procedure here, but interested readers are encouraged to review the details in B10, especially the caveats and warnings regarding the detection of faint X-ray sources. *Chandra*-ACIS event data were calibrated and cleaned as described in Section 3 of B10. Candidate point sources were then identified in the pointing using Lucy-Richardson image reconstructions (Lucy 1974) of small overlapping images that “tile” the field in three energy bands (0.5–7, 0.5–2, 2–7 keV). These candidate sources were then extracted using the most recent and improved version of the *ACIS Extract* (hereafter AE) software package¹ (Broos et al. 2012), which also uses the CIAO and MARX software (Fruscione et al. 2006; Davis et al. 2012). For each source, AE calculated the probabilities that the counts extracted in each of three energy bands arose solely from the local background. When all three probabilities were greater than 0.01 or when less than three X-ray counts were extracted, the candidate source was judged to be not significant, and removed from the list. The positions of surviving source candidates were updated with AE estimates, and the reduced list of candidates was re-extracted. This cycle of extraction, pruning, and position estimation was repeated until no candidates were found to be insignificant. Our final X-ray catalog contains 1026 individual point sources, 1022 of which are located in the field of view of the ACIS-I array, and 4 in the field covered by the single active ACIS-S chip.

The final list of X-ray sources with their properties is given in the electronic Table 1 (available at the CDS). Sources are identified by their sequence number (Col. 1) or their IAU designation (Col. 2). Following the rules for the designation of sources found with the *Chandra* X-ray Observatory, we have registered the acronym *CXONGC3293* as the prefix for the IAU designation (Col. 2).

The choice of the source significance limit (denoted “ProbNoSrc_{min}” in the text below and listed as P_B in Table 1) for the definition of the final sample of X-ray sources is always a compromise. A strict limit will miss true X-ray sources, whereas a more generous limit will enhance the risk of including spu-

¹ The *ACIS Extract* software package and User’s Guide are available at http://www.astro.psu.edu/xray/acis/acis_analysis.html.

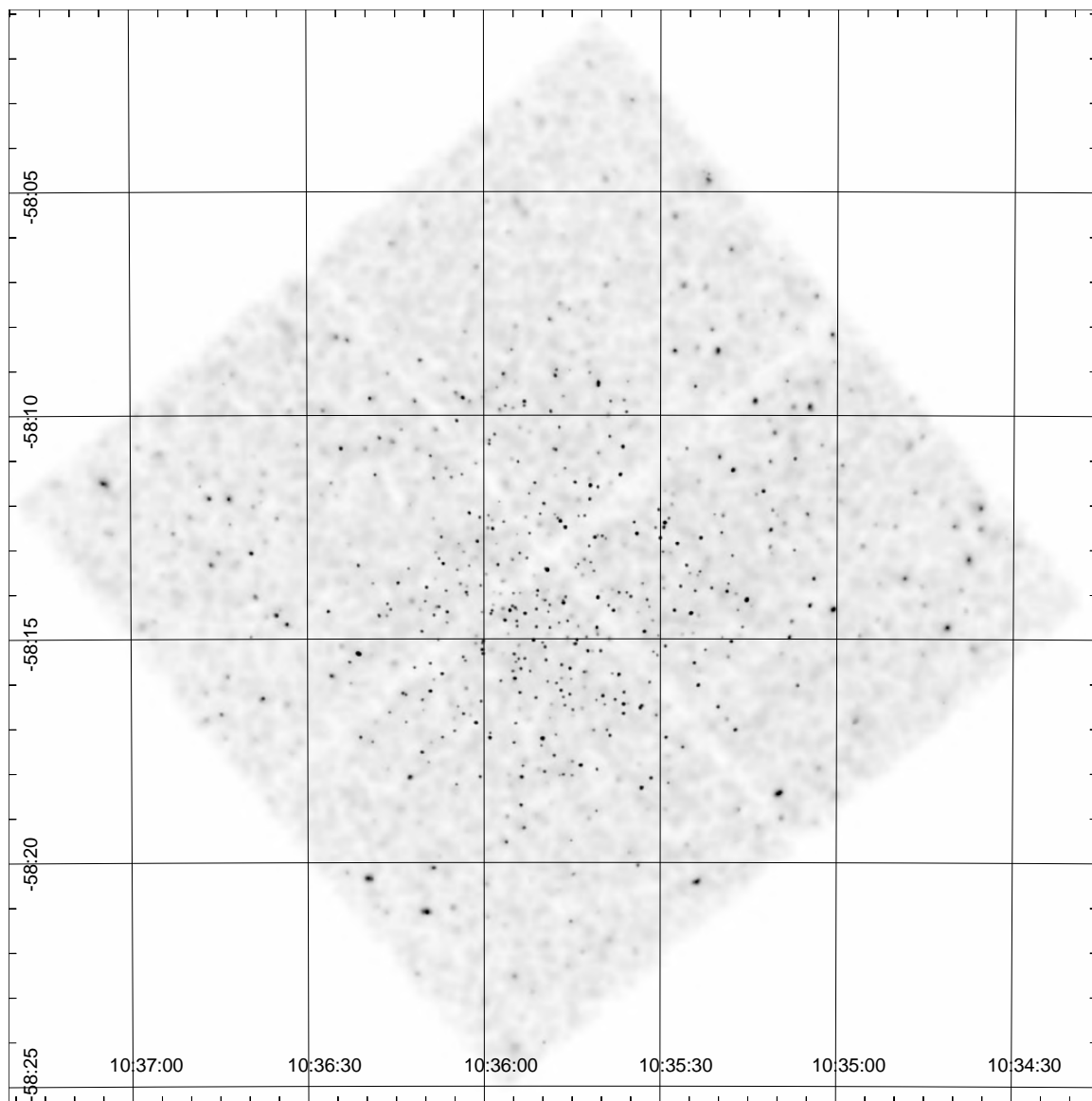


Fig. 2. Negative grayscale representation of the *Chandra* ACIS-I image for the total band (0.5 – 8 keV). The image was smoothed with the CIAO tool `csmooth` and is displayed with an `asinh` intensity scale. North is up and east to the left.

rious sources into the sample. The limiting value we use here ($\text{ProbNoSrc}_{\min} = 0.01$) tends to be on the generous side and allows the detection of sources with just ~ 3 counts. We note that the same value has been used in numerous similar *Chandra* studies of young stellar clusters (e.g., Feigelson et al. 2013), and in particular also in the CCCP (see Broos et al. 2011b, for a detailed discussion of the threshold value).

In order to keep track of the possible effects of potentially spurious sources on the analysis of the cluster properties in Sect. 4, we defined two subsamples of our source catalog. The first group comprises the very significant sources, defined as having a low probability of being a spurious source, ProbNoSrc_{\min} in Table 1 less than 0.003. This group contains 849 of the 1022 ACIS-I sources, which we refer to as “highly reliable” X-ray sources in the following text. The second group comprises the complementary set of 173 less significant ACIS-I sources ($0.003 < \text{ProbNoSrc}_{\min} < 0.01$), which we refer to as “less reliable” X-ray sources in the following text. In the analysis in

the following sections we check how the results change when we include or exclude the subsample of the less reliable X-ray sources. As shown there, we find that our derived quantitative results about the cluster properties are not significantly dependent on whether the less reliable X-ray sources are included or excluded.

2.2. X-ray variability

As part of the AE procedure, the time variability of each X-ray source is investigated by comparing the arrival times of the individual source photons in each extraction region to a model assuming temporal uniform count rates. The statistical significance for variability is then computed with a one-sided Kolmogorov-Smirnov statistic (Col. 15 of Table 1). In our sample, 29 sources show significant X-ray variability (probability of being constant $P_{\text{KS}} < 0.005$) and an additional 71 sources are classified as possibly variable ($0.005 < P_{\text{KS}} < 0.05$).

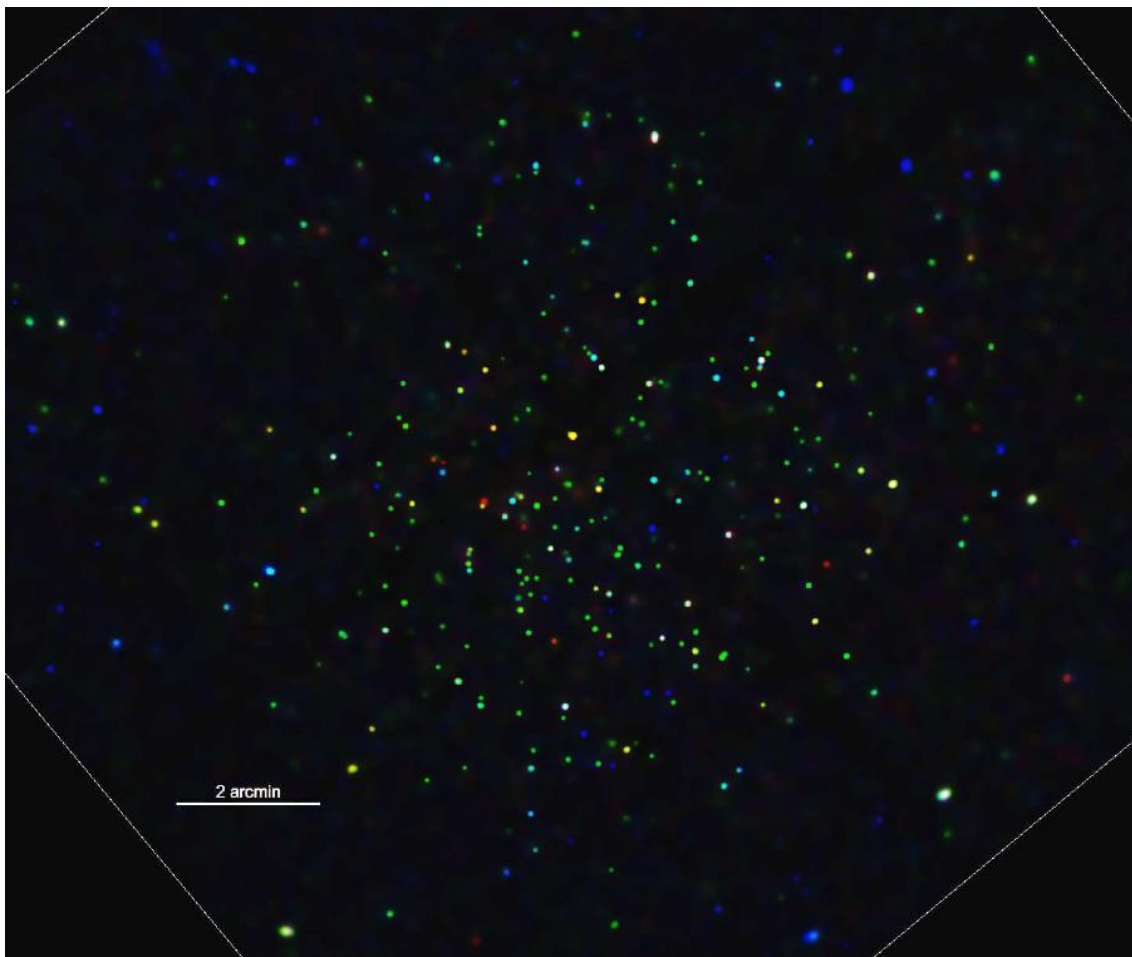


Fig. 3. RGB Color composite of the central part of the *Chandra* ACIS-I image in selected energy ranges (red: [0.5 – 1] keV, green: [1 – 2] keV, blue: [2 – 8] keV). The image was smoothed with the CIAO tool `csmooth` and is displayed with an asinh intensity scale. North is up and east to the left.

The light curves of the variable X-ray sources show a variety of temporal behaviors. Some sources show flare-like variability, i.e., a fast increase in the count rate followed by a slow exponential decay, which is typical of solar-like magnetic reconnection flares (see, e.g., Wolk et al. 2005). Other variable sources show more slowly increasing or decreasing count rates, as is often found for young stellar objects (see, e.g., Stassun et al. 2006).

2.3. X-ray spectral analysis for bright sources

Modeling the observed X-ray spectrum provides the best way to estimate the intrinsic X-ray luminosity of a source, but it requires a sufficiently large number of source counts. We restricted the spectral fitting analysis to 57 sources detected with $S/N > 4$.

XSPEC version 12.9.0i was used for this analysis. The background-subtracted spectra were grouped into bins of constant signal-to-noise ratio, and the fits were then performed using the χ^2 statistic. Considering the relatively small number of counts in our spectra, it is advisable to keep the number of free parameters as low as possible. We therefore only used one-temperature models², where the thermal plasma was described with the *VAPEC* model, and the *TBABS* model described the effect of extinction by interstellar and/or circumstellar material (as

² We tried spectral models with more than one temperature component for the brightest sources, but found that such more complicated models were not a statistical improvement on the one-temperature fits.

parameterized by the hydrogen column density N_{H}). The elemental abundances for the plasma model were fixed at the values³ that were found by Güdel et al. (2007) to be typical for young stellar objects.

In our fitting, the N_{H} parameter was allowed to vary between 10^{19} cm^{-2} and 10^{23} cm^{-2} and the plasma temperature kT between 0.1 and 10 keV. Since the parameter space of these fits can have a complicated topology rather than a clearly defined, unique minimum, we performed at least six fits for each source with different values of the starting parameters. The grid of starting parameter values is spanned by the vectors $N_{\text{H}} = [10^{21}, 10^{22}] \text{ cm}^{-2}$ and $kT = [0.3, 1.0, 3.0] \text{ keV}$. From the resulting fits, the model with the overall highest value of the null hypothesis probability was then selected as the global best fit. From the spectral fits we computed the intrinsic (i.e., extinction corrected) X-ray fluxes $F_{X,ic}$ for the total band (0.5 – 8 keV), as derived from the spectral fit parameters, and the corresponding X-ray luminosities $L_{X,ic}$, assuming a source distance of 2.3 kpc.

The derived plasma temperatures range from $\approx 3 \text{ MK}$ up to $\approx 85 \text{ MK}$ (for a star that exhibited a strong X-ray flare during our observation). The X-ray luminosities derived for the X-ray sources with infrared counterparts are in the typical ranges found

³ The adopted abundances, relative to the solar photospheric abundances given by Anders & Grevesse (1989), are: C = 0.45, N = 0.788, O = 0.426, Ne = 0.832, Mg = 0.263, Al = 0.5, Si = 0.309, S = 0.417, Ar = 0.55, Ca = 0.195, Fe = 0.195, Ni = 0.195.

for young stars in other star forming regions (see, e.g., Preibisch et al. 2005).

Owing to the moderate number of counts in most spectra, the uncertainties of the model parameters are often rather high. For many objects, the fitting analysis did not yield a clear unique best-fit model; two (or more) regions in the $N_{\text{H}} - kT$ parameter plane yielded very similar values for the best χ^2 . This ambiguity in the best-fit parameters can lead to substantial uncertainties in the derived X-ray luminosities. Furthermore, several fits hit the lower N_{H} limit, suggesting that the extinction is small, but leaving the value of N_{H} (and thus the un-absorbed X-ray luminosity) poorly constrained. We therefore decided to use the spectral fitting results only for those few sources for which reasonably well-defined best-fit parameters could be determined. These cases are described individually in the text below.

We note that the brightest ACIS-I X-ray source (number 943; 190 net counts) is a special case: it has no optical counterpart, only an extremely faint infrared counterpart, and a very hard X-ray spectrum that can be well fit by a power-law model. As described in more detail in Appendix D, these properties suggest it to be an extragalactic source, most likely an obscured quasar.

2.4. X-ray fluxes for fainter sources

Since the large majority of the detected X-ray sources is too faint for meaningful spectral fitting analysis, we need another way to estimate the intrinsic X-ray luminosities. In the course of the AE analysis, an estimate of the incident energy flux onto the telescope is calculated for each source. However, these flux values are known to be biased because their computation is based on the (non-physical) assumption of a flat incident spectrum, which is not correct for most X-ray sources.

For the X-ray sources that are identified with cluster stars, we can improve the accuracy of the flux estimate by using the available a priori information on the typical shape of X-ray spectra of young stars. We can also use the available constraints on the extinction (individual extinction estimates available for the B-type stars, or an empirical mean value for the extinction) and estimate not only the apparent, but also the intrinsic (i.e., absorption corrected) X-ray fluxes and thus the X-ray luminosities of these stars. For this, we employed the `srcflux` tool⁴ in the *Chandra Interactive Analysis of Observations* (CIAO) software package. This tool determines the conversion factor from count rate to apparent as well as unabsorbed energy flux for a given spectral model, creating ARFs and RMFs for each source. It is necessary to specify a model for the X-ray spectrum and for the X-ray absorption caused by the ISM along the line of sight. We used a thermal plasma spectrum with a plasma temperature of $kT = 1$ keV, which is a typical value for young coronally active stars (see Preibisch et al. 2005). For the absorption we used the model `xsphabs` and set the column density to $N_{\text{H}} = 0.15 \times 10^{22} \text{ cm}^{-2}$; this corresponds to a visual extinction of $A_V \approx 0.75$ mag, which is the mean value of the individual extinctions determined for the bright cluster stars.

3. Infrared and optical counterparts of the X-ray sources

The identification of optical/infrared (OIR) counterparts of the X-ray sources is required in order to obtain essential information about the nature and properties of the X-ray emitting objects, in

particular to discern between stellar X-ray sources and (mostly extragalactic) contaminants.

The number of expected extragalactic contaminants can be estimated by comparing the point-source sensitivity of our ACIS-I image to the cumulative number counts of AGN found in the *Chandra* Deep Field South project (see Lehmer et al. 2012). This suggests $\approx 120 - 140$ AGN among the detected X-ray sources. X-ray source 943, described in Appendix D, seems to be the X-ray brightest of these extragalactic X-ray sources. A large fraction of the OIR counterparts of these extragalactic X-ray sources are expected to be too faint to be detected in our OIR images.

Stellar X-ray sources, on the other hand, should have relatively bright OIR counterparts. The expected optical and infrared magnitudes of young low-mass stars of NGC 3293 can be easily estimated. Assuming an age of about 10 Myr and a typical extinction of $A_V \approx 1$ mag, stars with masses of $[1.0, 0.5, 0.1] M_{\odot}$ are predicted to have visual magnitudes of $V \approx [19.0, 20.8, 25.9]$ and NIR magnitudes of $H \approx [16.0, 16.4, 18.3]$ according to the pre-main-sequence stellar models of Siess et al. (2000). These numbers show that typical optical images are not sensitive enough to detect the full low-mass population in NGC 3293. In the NIR regime, these low-mass stars are much easier to detect, but nevertheless too faint to be contained in all-sky catalogs such as the 2MASS data.

3.1. VISTA near-infrared images and point source catalog

As the main source for the identification and infrared characterization of the X-ray sources we used the images and the point source photometric catalog from our VISTA Carina Nebula Survey (VCNS), which is described in detail in Preibisch et al. (2014b). These VISTA data provide subarcsecond resolution and 5σ point-source sensitivities to $[J, H, K_s] \approx [20, 19.5, 18.5]$ mag. Comparing these magnitude limits to the above mentioned expected magnitudes of low-mass stars in NGC 3293 shows that the VISTA data are clearly deep enough to detect all low-mass members of the cluster, i.e., down to $0.1 M_{\odot}$, and even through several magnitudes of visual extinction. There are 35 143 VISTA catalog sources with valid photometry in all three NIR bands in the ACIS-I field of view. Five extremely bright stars in the cluster are so heavily saturated in the VISTA images that they were not recognized as point sources in the VISTA data processing; for these five stars (with magnitudes between $J = 3.5$ and $J = 8.5$), positions and magnitudes from the 2MASS point source catalog were used.

Like any large-scale catalog, the VISTA catalog is not 100% perfect and complete. As described in Sect 3.2 of Preibisch et al. (2014b), some point-like objects, which are clearly visible in the VISTA images, are missing from the catalog. This problem is mostly restricted to areas close to very bright stars where the wings of the point spread function and numerous diffraction spikes produce a bright and spatially variable background pattern⁵, and also concerns close companions to some stars. This sample of additional infrared sources is considered separately after the matching with the VISTA catalog as described below in Sect. 3.4.

⁵ The $\sim 1'$ area around the star V361 Car in the VISTA image shown in Fig. 4 provides a good example of this effect.

⁴ see <http://cxc.harvard.edu/ciao/ahelp/srcflux.html>

3.2. Optical images and catalog from VST

We used optical images of NGC 3293 that were obtained with Omegacam at the ESO 2.6 m VLT Survey Telescope (VST; Kuijken 2011) in the u -, g -, r -, i -SDSS filters and an $H\alpha$ filter as part of the VPHAS+ survey (Drew et al. 2014). The 5σ detection limits in these images are approximately $u = 20.5$, $g = 22.5$, $r = 21.4$, and $i = 20.5$ (all magnitudes in the Vega system).

The ESO archive contains the fully reduced, calibrated, and verified Phase 3 data products from this survey. We downloaded all reduced images covering NGC 3293, and also retrieved the VPHAS-DR2 Point Source Catalogue data for this area, which provide band-merged PSF and aperture photometry for the point-like objects (“primary sources” in the VPHAS+ terminology). 8581 of these VST primary sources are in the ACIS-I field of view. The g -band magnitudes of these stars range from $g \approx 12.6$ (close to the saturation limit) down to $g \sim 23$. Comparing this faint magnitude limit to the above mentioned expected magnitudes of low-mass stars in NGC 3293 shows that the VST data should detect most lightly absorbed ($A_V \lesssim 1$ mag) low-mass members of the cluster down to $\gtrsim 0.5 M_\odot$, but will miss many of the lower-mass members and also stars with visual extinction of more than about one visual magnitude. The B-type and most A-type stars in NGC 3293 are also missing from the catalog, due to the saturation limit. For these bright stars, optical photometry is available from Baume et al. (2003) and Dufton et al. (2006).

We note that the VST catalog suffers from a similar incompleteness to that of our VISTA catalog, in the sense that some point-like objects that are clearly visible in the images are missing from the catalog. Another limitation of the VST images is that many of the very bright stars in the cluster center are strongly saturated in the CCD images. The bleeding streaks caused by these saturated stars extend up to 1.5 arcmin in two directions from each saturated source, and have widths up to about 20 pixels. In the central ~ 10 square arcmin region, these bleeding streaks cover a significant fraction of the image area. Faint sources may be completely hidden behind these bleeding streaks. A visual inspection of the VST g -band image showed that at least 12 X-ray sources are located at positions within or just at the edge of such a bleeding streak or other image artifacts, which prevents the identification of optical counterparts. No attempt was made to construct a list of point sources missing from the VST catalog; the matching analysis was restricted to the VPHAS catalog sources only.

3.3. Further optical photometry and spectral data

Our master catalog (based on the VISTA point source catalog) was complemented by the optical (UBVRI $H\alpha$) photometry catalog for NGC 3293 from Baume et al. (2003), which provides V -band magnitudes (down to $V \sim 20$) for 1690 stars in the cluster and optical colors for a subset of them.

We also added information available in the literature about the spectral and other stellar parameters of stars in NGC 3293 into our catalog. Most of these data originate from the VLT-FLAMES multi-object spectroscopic survey of massive stars in NGC 3293 (Evans et al. 2005; Dufton et al. 2006), which provided spectral types for 131 stars and luminosities for 92 of these. In the ACIS-I field of view, our final catalog lists 97 B-type stars, 17 A-type stars, 2 F-type stars, and 1 M-type star (the M1.5 Iab supergiant V361 Car).

3.4. Matching of the X-ray sources with the optical/infrared catalogs

Figure 4 shows a NIR image of the central part of the cluster with the polygons of the X-ray source extraction regions overlaid. The high density of point-like sources in the NIR image (which is largely due to the strong galactic background at the cluster’s position very close to the galactic plane) shows that a proper identification of the counterparts to our X-ray sources requires a careful and conservative matching procedure in order to avoid false matches with unrelated background objects.

The identification of infrared and optical counterparts to the X-ray sources was performed with a two-step procedure: an automatic source matching based on catalog coordinates, followed by a detailed individual inspection in order to resolve problematic cases such as multiple possible matches or objects missing from the optical/NIR catalogs.

For the first step, we employed the IDL tool⁶ `match_xy`, as described in Broos et al. (2011b). The maximum acceptable matching separation between an X-ray source and a counterpart was based on the individual source position errors assuming Gaussian distributions, scaled so that $\sim 99\%$ of the true associations should be identified as matches. For the X-ray sources, the positional uncertainties were determined by AE, and for the VISTA and VST sources we assumed position uncertainties of $0.1''$. The algorithm in `match_xy` lists the most significant match of each X-ray source as its “Primary Match”, while any other possible significant matches, if present, are considered “Secondary Matches”. In a second stage, the algorithm resolves possible many-to-one and one-to-many relationships between the X-ray and infrared/optical catalogs. Clear one-to-one relationships are classified as “successful primary matches”, while in cases where, e.g., two X-ray sources are significantly close to a single infrared source, the less significant primary match is labeled as “failed”. This finally provided a reasonable one-to-one set of matches, consisting of 695 successful primary matches to VISTA catalog sources in the ACIS-I field.

For 42 X-ray sources, one or more successful secondary matches were identified by `match_xy` in the VISTA catalog. These cases require further inspection since it is not guaranteed that the closest match is always the correct physical counterpart, due to the high surface density of infrared sources in our deep VISTA images. Instead, a physically unrelated (e.g., background) infrared source may appear in the matching region just by chance and produce a “false match”, and might even degrade the true infrared counterpart to a secondary match. A priori information about the typical infrared properties of X-ray detected young stars can be used to identify possible cases where this problem occurs. Since we observe a young stellar cluster and know from the X-ray detection limit that most of the X-ray detected objects should be young stars with masses of $\gtrsim 0.5 M_\odot$, these stars should typically be relatively bright NIR sources. Therefore, all cases where an X-ray source has an unexpectedly faint primary match and a considerably brighter secondary match (i.e., with the magnitudes expected for a young star) deserve special attention. We found eight such cases, and replaced the original faint primary match by the considerably brighter secondary match.

As the last step in the source matching procedure, we finally considered the above mentioned list of point-like sources identified in our visual inspection of the VISTA images but missing from the VISTA source catalog. The locations of these additional VISTA sources were compared to the X-ray source locations for

⁶ see www2.astro.psu.edu/xray/docs/TARA/TARA_users_guide/node11

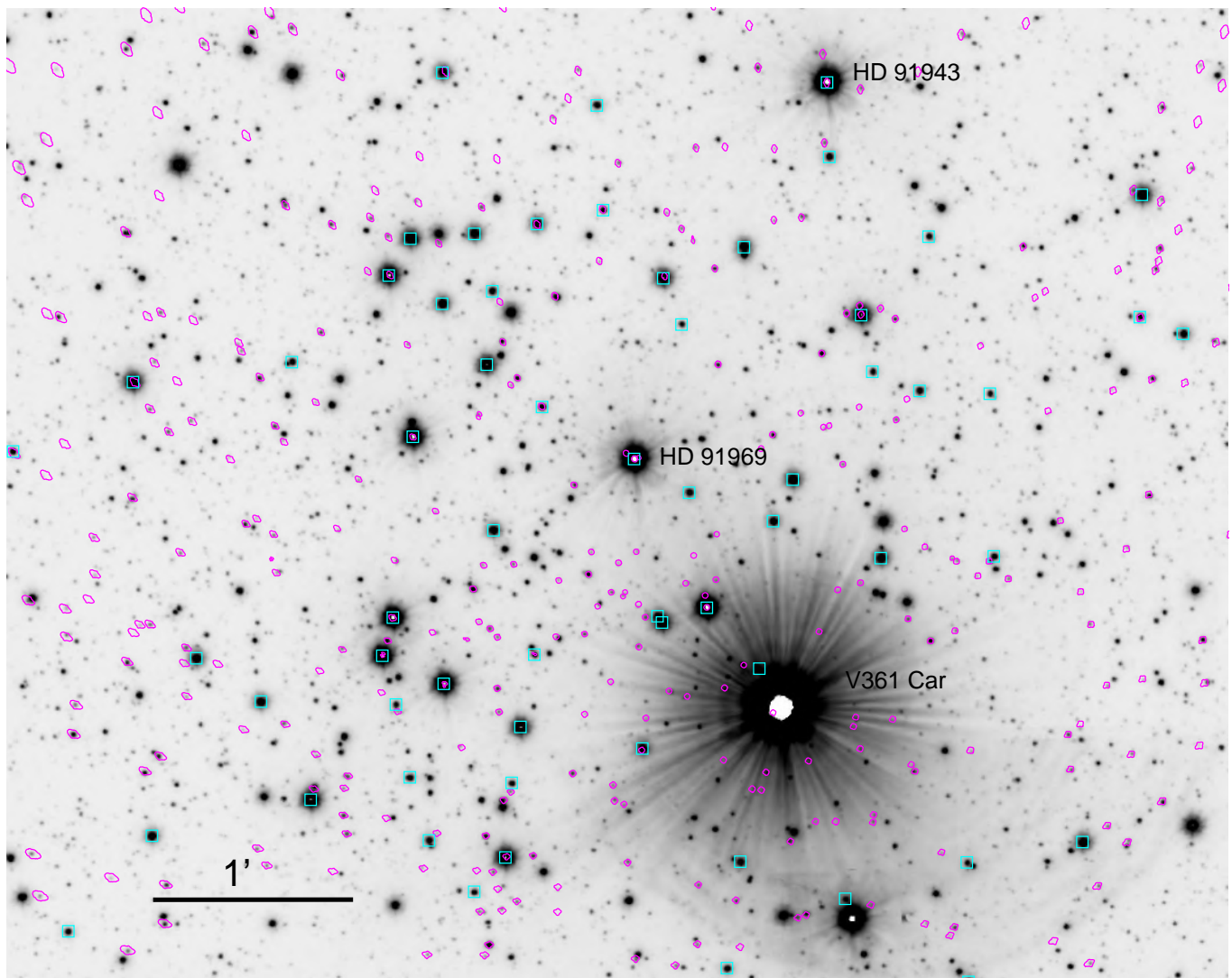


Fig. 4. VISTA *H*-band image of the central part of NGC 3293. North is up and east to the left. The known B-type stars are marked by the cyan squares. The *Chandra* X-ray sources are marked by their individual source extraction polygons drawn in magenta. The M1.5Iab supergiant V361 Car, the B0 Iab star HD 91969, and the B0.7 Ib star HD 91943 are labeled.

which `match_xy` did not report a match with a VISTA catalog star. In this way, 61 additional infrared point source matches to *Chandra* sources were identified. We note that most of these 61 additional infrared sources have discernible counterparts in the optical VST images, and 20 of them are even listed as point sources in the VST catalog, demonstrating the reality of these infrared sources.

Since most of these objects are affected by a spatially variable background or by partial blending with other nearby sources in the VISTA images, measurements of their photometry can suffer from relatively large uncertainties. In order to quantify these uncertainties, we performed aperture photometric measurements in the VISTA images, employing different values for the sizes of the background regions, and determined the scatter of the resulting aperture flux measurements for each source. For 21 of these sources, the relative scatter of these flux measurements exceeded 20%; these sources were completely excluded from all further analysis steps. For the 40 sources for which the relative scatter of the flux measurements was less than 20%, we determined their magnitudes, but these sources were not included in the sample of VISTA catalog sources; they are considered in some of the analysis steps below, but are always clearly kept separate from

the VISTA catalog sources. There is thus no danger that these additional sources will contaminate our results.

In the matching with the VST optical catalog, we considered all sources that are listed as primary source in the VPHAS-DR2 catalog. The matching with the VST catalog resulted in 496 successful primary matches in the ACIS-I field. In the course of our visual inspection of the X-ray source positions in the VST images, we found one case where an image artifact that was erroneously listed as point source in the VPHAS-DR2 catalog coincided with an X-ray source. More details about this artifact are given in Appendix C.

The final results of the matching procedure can be summarized as follows: 756, i.e., 74.0 % of all X-ray sources in the ACIS-I field, have a match with a VISTA source (695 of them, i.e., 68.0%, with a VISTA catalog source). For the VST catalog, we have 491 matches of VST catalog primary source to ACIS-I X-ray sources after removing the above mentioned artifact, and four cases where the VST match was not identical to the VISTA match; this yields a match fraction of 48.0%. The lower rate of counterparts in the VST catalog is easily understood as a consequence of the different sensitivity limits of the two catalogs.

While the VISTA catalog is deep enough to detect $0.1 M_{\odot}$ stars in NGC 3293 with extinctions up to $A_V \approx 5$ mag, the sensitivity limit of the VST catalog corresponds to $1 M_{\odot}$ stars with extinctions up to $A_V \approx 3.5$ mag, or $0.5 M_{\odot}$ stars with extinctions up to $A_V \approx 2$ mag. Therefore, most of the $< 0.5 M_{\odot}$ stars and a substantial fraction of the $[0.5 - 1] M_{\odot}$ stars remain undetected and will be missing from the VST catalog.

Information about the VISTA and VST matches to the individual X-ray sources is contained in the electronic Table 2, available at the CDS.

Finally, we can compare the fraction of IR matches for the two above-mentioned subsamples of our X-ray catalog. In the sample of 849 highly reliable ACIS-I sources, we find 593 objects (i.e., $69.8 \pm 0.2\%$) that have a match with a VISTA catalog source. In the less reliable sample, 102 of the 173 ACIS-I sources (i.e., $59.0 \pm 3.7\%$) have a VISTA catalog match. The lower match fraction for the less reliable subsample is partly due to a higher fraction of spurious sources among the less reliable sources. It should be noted, however, that X-ray sources detected with lower significance generally have weaker X-ray fluxes. Since there is some correlation between X-ray flux and infrared brightness for most classes of X-ray emitting objects, the less significant true X-ray sources are also less likely to have an infrared counterpart that is detected in the available infrared images.

3.5. Reliability of X-ray sources and their infrared matches

In order to determine the reliability of the following analysis, we briefly discuss a few fundamental aspects of the sample of X-ray sources and their OIR matches. In general, any X-ray source list is composed of real sources and spurious sources. Concerning the identification of OIR matches to the X-ray sources, it is necessary to take into account that brighter sources are usually detected with higher significance, i.e., there is a correlation between X-ray source brightness and significance. There is also a correlation between X-ray flux and OIR brightness for most classes of X-ray emitting objects; therefore, the less significant true X-ray sources are, on average, fainter in the OIR range and therefore also less likely to have a counterpart that is detected in the available OIR images.

For the OIR counterparts of the real X-ray sources there are two possibilities: some of the X-ray sources can be expected to have a counterpart bright enough to be detected in the available OIR images (in the present study, this concerns all young stars in NGC 3293 in the deep VISTA images, and the $\geq 1 M_{\odot}$ stars in the VST images). Another fraction of the X-ray sources will be extragalactic objects (mainly AGN), most of which should be very faint at OIR wavelengths and thus remain undetected in the available OIR images.

If we now consider the possible results of the X-ray to OIR source matching, we have to distinguish four possibilities for the real X-ray sources: (a) *correct positive matches*, when the physical association between an X-ray source and the corresponding OIR source is correctly identified; (b) *correct negative matches*, when an X-ray source is not matched to any OIR catalog source because the OIR counterpart is too faint to be detected in the OIR images; (c) *false negative matches*, when the true OIR counterpart is not considered a match, e.g., because the angular distance of the catalog entry is wider than the matching limit; and (d) *false positive matches*, when unassociated objects are incorrectly considered a match, e.g., because the catalog coordinates of some unrelated OIR source are by chance closer to the X-ray source position than the coordinates of the true counterpart, or because the true counterpart is undetected in the available OIR images

and an unrelated OIR source is close enough to the X-ray source position.

For the spurious X-ray sources, there are two possibilities: (e) *correct negative matches*, when no OIR counterpart is associated with the non-existing X-ray source, and (f) *false positive matches*, when an unrelated OIR source is wrongly considered to be a match to the non-existing X-ray source.

In any matching procedure, some level of spurious matching will inevitably occur. These issues were discussed in detail in Broos et al. (2011b), where quantitative estimates for the expected numbers of false positive matches with random unrelated infrared sources were derived for the case of the CCCP data set. However, the numbers for the expected fractions of false positive matches derived by Broos et al. (2011b) cannot be directly applied to the present study because the underlying infrared catalogs are quite different. The highest estimated false match fraction derived in Broos et al. (2011b) was based on the matching of the CCCP X-ray source list with the very deep HAWK-I infrared catalog (see Preibisch et al. 2011b). Since the HAWK-I catalog is about 2 magnitudes deeper (i.e., a factor of ≥ 6) than the VISTA catalog we use here, it contains a large number of very faint (mostly background) objects that provide numerous possibilities for random false positive matches; however, these very faint objects remain undetected in the VISTA catalog and thus cannot produce random false positive matches in our case. Since the HAWK-I catalog lists on average ≈ 470 IR sources per square-arcminute in the CCCP field, while the VISTA catalog contains only 140 sources per square arcminute in the NGC 3293 region, the probability of obtaining a random false positive match with the VISTA catalog is at least about 3 times lower than reported for the HAWK-I catalog in the CCCP field.

In order to derive a quantitative estimate for the occurrence rate of random false positive matches for X-ray sources in our NGC 3293 data set, we performed a set of random matching simulations that are described in Appendix B. These simulations show that the average probability that a spurious X-ray source will get a false positive VISTA catalog match is about 23%. It is very important to note that this is not equal to the expected fraction of false matches in our sample since in reality a large fraction of our X-ray sources are true sources that have a counterpart in one of the young stars in NGC 3293; the 23% probability for false positive matches applies only to the subset of X-ray sources that have no true physical counterparts in our VISTA images, which is considerably smaller than the full sample.

In order to estimate the possible consequences of such false positive matches on the results of our study of the cluster properties described below, it is important to note that the large majority of all random false positive matches are with very faint IR sources. This is just a consequence of the fact that the number of IR sources increases strongly when going towards fainter magnitudes. The majority of the VISTA catalog sources in the NGC 3293 field have magnitudes $J > 18.5$. False matches with such very faint IR objects will only have very minor effects on our analysis of the color magnitude diagram presented below; e.g., such very faint IR objects cannot be confused with $M \geq 1 M_{\odot}$ cluster stars, which are considerably brighter. Most of our X-ray sources with VISTA catalog matches are much brighter and have magnitudes $J < 16.5$. As shown in Appendix B, the probability of a random X-ray source obtaining a false positive match with a VISTA catalog source brighter than $J = 17$ [$J = 16$] is just 4.6% [2.5%].

If we assume that $\approx 20\%$, i.e., ≈ 200 of the sources, in our X-ray catalog have no physical counterparts in the VISTA images

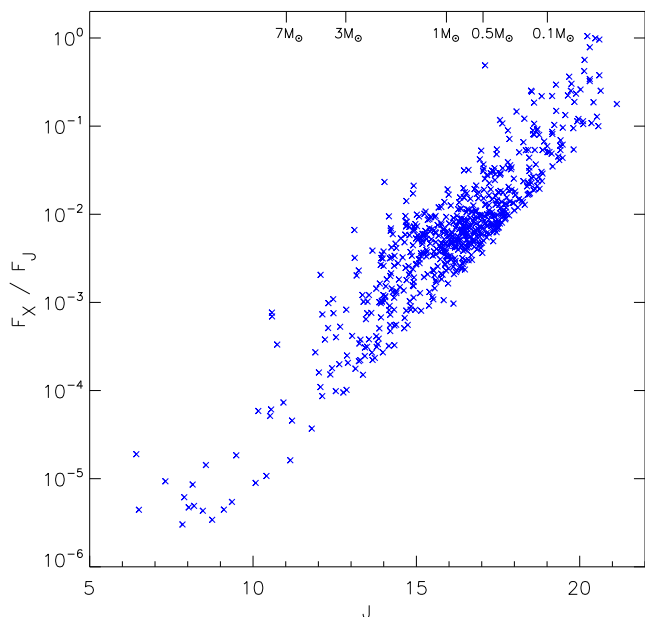


Fig. 5. Ratio of observed X-ray fluxes to observed J -band fluxes plotted against the J -band magnitudes of the X-ray sources with infrared counterparts. On the upper x-axis, the expected J -band magnitudes for 10 Myr old stars with different masses are indicated according to the models of Siess et al. (2000).

(i.e., they might be spurious sources), we expect there will be ≈ 46 false positive matches with VISTA catalog sources. However, only $\approx 5-9$ of these would be false positive matches to stars that are bright enough ($J \leq 16-17$) to possibly affect our star counts for the investigation of the cluster IMF presented in Sect. 4.3.5.

4. Exploring the cluster properties

Our X-ray selected sample provides the first opportunity to study individually identified low-mass stars in NGC 3293. We first consider the X-ray-to-infrared flux ratios of the objects, and then use color magnitude diagrams (CMDs) to derive information about the ages and masses of the X-ray detected stars and information about the size of the low-mass star population in the cluster.

4.1. X-ray and infrared fluxes

Reliable bolometric luminosities (i.e., determined from spectroscopic information) are only available for a relatively small number of stars in NGC 3293 (essentially the B-type stars, which we discuss in Sect. 5). For the bulk of the stellar population of NGC 3293, we thus cannot directly determine the ratio of X-ray to bolometric luminosity, which would be a good diagnostic of the nature of X-ray emission. Therefore, we employ here the observed J -band flux as a proxy for the stellar luminosity. For late-type stars, the J -band flux is roughly proportional to the stellar bolometric luminosity; furthermore, the influence of extinction is rather small in the J -band ($A_J \approx 0.28 \times A_V$).

In Fig. 5 we show the ratio of observed X-ray and infrared fluxes for the sources in NGC 3293, which shows that the majority of X-ray detected sources are objects for which their J -band magnitudes suggest stellar masses in the range $\sim [2-0.5] M_\odot$, consistent with the X-ray sensitivity limit. Most of the stars in the range $J \approx [14-18]$ show ratios around a typical value

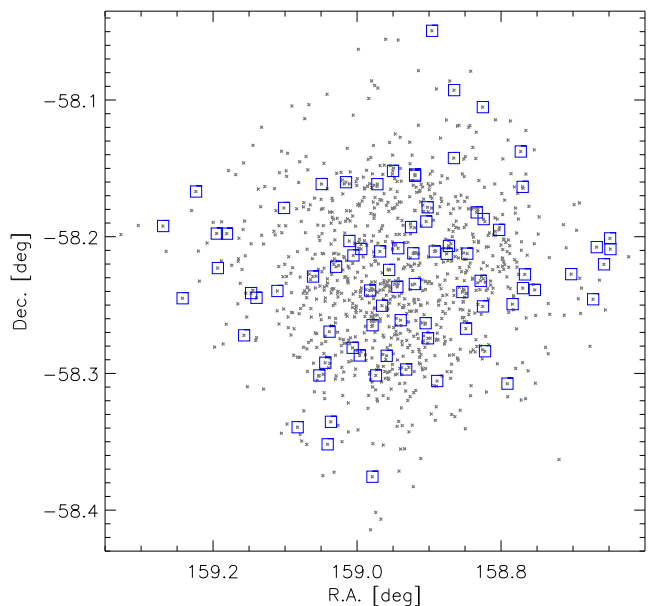


Fig. 6. Spatial distribution of the X-ray sources. The small gray crosses show all X-ray sources. The blue squares mark the spatially complete sample of sources with an observed X-ray photon flux $\log F_{r,\text{photon}} > -5.9$ photons $\text{s}^{-1} \text{cm}^{-2}$ that have VISTA counterparts with $J < 18$.

of $\log(F_X/F_J) \approx -2.2$. Since for these low-mass stars, the bolometric flux is roughly a factor of ~ 10 higher than the J -band flux, this corresponds to fractional X-ray luminosities of $\log(L_X/L_{\text{bol}}) \approx -3.2$, which is the typical ratio for coronally active young low-mass stars.

The bright stars in the range $J \approx [6-9]$ show typical ratios $\log(F_X/F_J) \approx -5.2$. Since for early B-type stars, the bolometric flux is typically a factor of ~ 1000 higher than the J -band flux, this translates roughly into $\log(L_X/L_{\text{bol}}) \approx -8.2$. Again, this is very consistent with the results from other studies (e.g., Stelzer et al. 2005; Gagné et al. 2011). A more accurate assessment of the X-ray properties of the B-type stars in NGC 3293 is given in Sect. 5.

Some of the faintest infrared sources ($J \gtrsim 19$) show very high X-ray-to-infrared flux ratios; many of these objects are probably extragalactic sources.

4.2. Spatial distribution of the X-ray sources

Next we consider the spatial distribution of the X-ray sources with the aim to derive information about the cluster size. Slawson et al. (2007) estimated the coronal radius of NGC 3293 to be $\sim 5.5'$, but since this was based on optical data that are not sensitive enough to detect the full cluster population (especially in regions where the extinction is more than $A_V \approx 1$ mag), an independent check is useful. We can address the question regarding the cluster size with our X-ray sample and with the deep VISTA images.

Considering the *Chandra* data, it should be noted that the sensitivity level of the observation is not uniform across the observed field since the point-source sensitivity drops significantly with off-axis angle. The most important factors that play a role here are the mirror vignetting and the degradation of the point spread function, both of which reduce the local sensitivity with increasing off-axis angle. Following the strategy of Feigelson et al. (2011), a “spatially complete sample” of X-ray sources can be constructed by employing a limit to the observed pho-

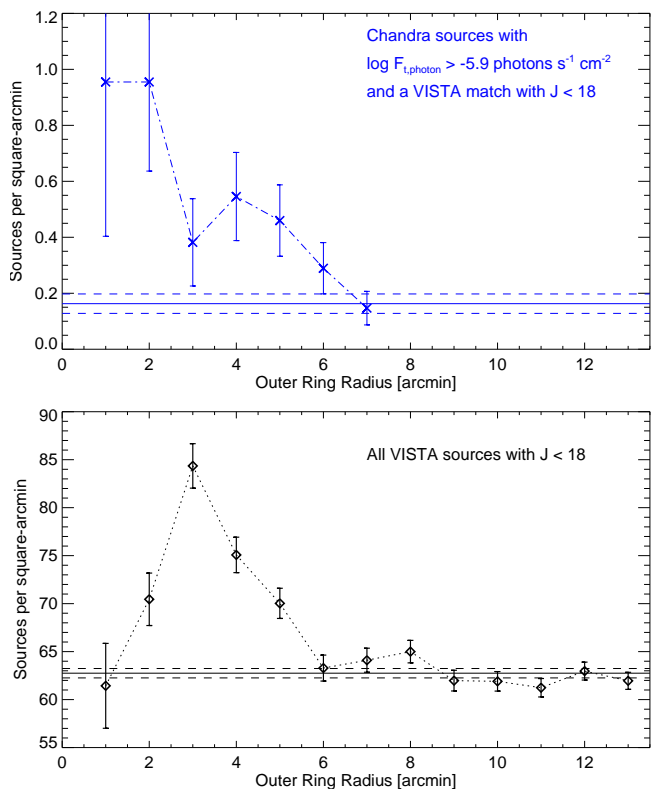


Fig. 7. Top: Radial profile of the surface density of *Chandra* sources in the spatially complete sample that have a VISTA match with $J < 18$ in different rings around the optical cluster center. The horizontal blue line and the parallel dashed lines show the mean value and the uncertainty of the source density outside the 7 arcmin region. Bottom: Radial profile of the surface density of all VISTA source with $J < 18$ in different rings around the optical cluster center. The horizontal line and the parallel dashed lines show the mean value and the uncertainty of the source density in several comparison fields.

ton flux of the X-ray sources that is high enough to make sure that sources above this limit can be detected in the full ACIS-I field of view, i.e., even at the edge of the X-ray image. This threshold on the observed X-ray photon flux is $\log F_{l,\text{photon}} > -5.9$ photons $\text{s}^{-1} \text{cm}^{-2}$.

Since we intend to trace the spatial structure of the stellar cluster, we use only those objects in this spatially complete X-ray sample that have a match with a VISTA source with $J < 18$, as expected for the large majority of X-ray detected young stars in NGC 3293. This final sample contains 81 sources. A map of the positions of these sources is shown in Fig. 6.

We determined the surface-density of these X-ray sources as a function of distance from the optical cluster center by counting the number of objects in concentric annular regions with different radii. The resulting radial profile is shown in the upper part of Fig. 7. The source density in the center is more than 5 times higher than in the outer parts of the ACIS-I image, drops with angular distance from the cluster center, and merges to the background value at an angular distance of $\approx 6-7$ arcmin from the center. This profile is consistent with the above mentioned previous estimate of the cluster radius and confirms that the ACIS-I field of view covers the full area of the cluster.

The question about the spatial extent of the cluster can also be addressed with the VISTA data. These data have several advantages. First, they cover a considerably larger area around NGC 3293 (the angular distance from the cluster center to the

nearest edge of the VISTA image is 12 arcmin). This makes it easy to define background comparison regions at angular distances of ≥ 10 arcminutes for a reliable computation of the background source density. Second, the VISTA images do not suffer significantly from PSF degradation and mirror vignetting, i.e., they provide a more homogeneous coverage of the observed area. Third, the VISTA data are sensitive enough to detect all cluster stars (down to $0.1 M_{\odot}$, and even through substantial extinction of $A_V \approx 5$ mag) and thus provide much larger source numbers and consequently better statistics in the source counts. However, there is also one disadvantage: several of the very bright stars in the cluster are saturated, and their PSF-wings and diffraction spikes create a high and complicated background halo around them, which severely restricts the detection of faint sources.

The radial profile of the surface density of all VISTA sources with $J < 18$ is shown in the lower part of Fig. 7. A clearly enhanced source density can be seen for radial distances between 2 arcmin and 6–8 arcmin from the cluster center. The low density in the center is caused by the strongly reduced detection efficiency for faint sources near the very bright stars in the cluster center. The VISTA density profile suggests a cluster radius in the range 6–8 arcmin.

Considering all these numbers together, a good estimate for the angular size of the cluster is ≈ 7 arcmin, which corresponds to ≈ 4.7 pc at 2.3 kpc distance.

4.3. Analysis of the color magnitude diagrams

In order to obtain information on the stellar properties of the X-ray detected stars, we constructed color magnitude diagrams (CMDs) and compared the location of the X-ray selected objects to the recent PARSEC stellar evolution models described in Marigo et al. (2017).

4.3.1. Near-infrared color magnitude diagram

In Fig. 8 we show the J versus $J - H$ color magnitude diagram of the X-ray detected objects in NGC 3293. The range of J -magnitudes is restricted to the fainter values in order to show the location of the low-mass stars more clearly; the color magnitude locations of the brightest (i.e., the early-type) stars can be seen in Fig. 9 and are discussed below.

The large majority of the X-ray selected objects are at CMD locations corresponding to stellar masses in the $[0.5 - 2] M_{\odot}$ range, as expected from the X-ray detection limits, and extinctions of a few visual magnitudes.

At the bottom of the CMD ($J \gtrsim 19$), the X-ray selected objects show a wide range of colors consistent with background objects and the expected locus of extragalactic sources.

4.3.2. Optical color magnitude diagrams

The construction of an optical CMD is not as straightforward as the NIR CMD described above, due to the sensitivity and saturation limits of the available optical images. The optical photometry catalog of Baume et al. (2003) is reported to become incomplete at $V = 16$, i.e., it will obviously miss a large fraction of the low-mass stars of NGC 3293. The VST catalog from the VPHAS+ survey is considerably deeper, but misses all stars brighter than $g \approx 13$, due to saturation effects. Another problem is that these two catalogs use different photometric systems, $UBVRI$ for Baume et al. (2003) and SDSS $ugri$ for VPHAS+.

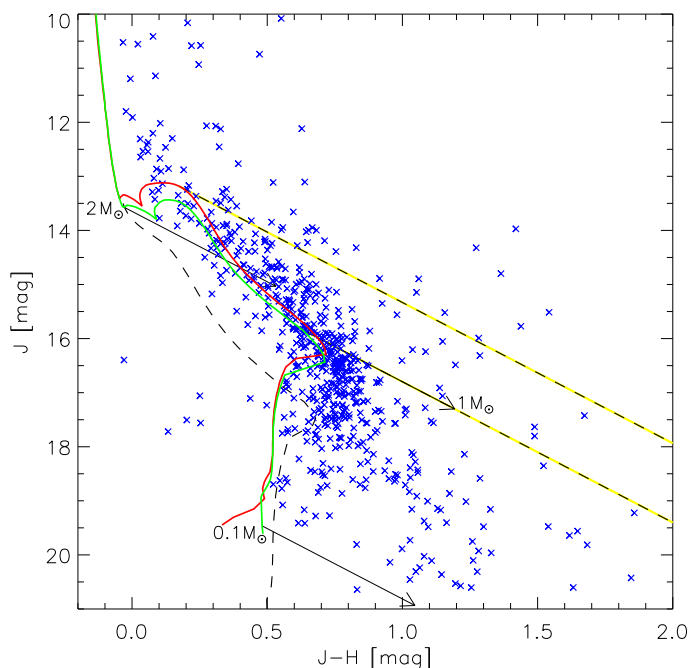


Fig. 8. Near-infrared color magnitude diagram of the X-ray detected objects in NGC 3293 (blue crosses). The red and green solid lines show isochrones for stellar ages of 8 Myr and 10 Myr, based on the PARSEC stellar models (Marigo et al. 2017). The black dashed line indicates the main sequence. The arrows indicate reddening vectors for $A_V = 5$ mag starting at the location of 10 Myr old stars with masses of $2 M_\odot$, $1 M_\odot$, and $0.1 M_\odot$. The yellow-and-black dashed lines show the upper and lower limits for the ranges that were used for counting the number of stars in the $[1 - 2] M_\odot$ interval.

We therefore consider the bright and the faint parts of the optical CMD separately.

The upper plot in Fig. 9 shows the bright part of the CMD, based on the Baume et al. (2003) data. All stars with $V \lesssim 9$ (i.e., the most luminous early B-type stars) are detected in X-rays. This matches the expectations since these very bright objects are the most luminous early B-type stars, which are expected to be strong X-ray emitters because they have quite strong stellar winds and their X-ray luminosity is correlated to their bolometric luminosity (see Gagné et al. 2011). At somewhat fainter magnitudes, in the range $V \approx [9-13]$, only a small fraction of the stars are detected in X-rays; this range corresponds to stars with late B and A spectral types, which are not expected to be intrinsic X-ray emitters. A star-by-star discussion of the individual X-ray properties and the observed trends of X-ray emission as a function of spectral type and stellar mass in the B- and A-type range is provided in Sec. 5. At fainter magnitudes, $V \gtrsim 13$ (corresponding to stellar masses $\lesssim 3 M_\odot$), the number of X-ray detected stars increases strongly, as expected for a stellar mass function that rises towards lower masses.

4.3.3. Age of the low-mass population

As can be seen in Fig. 8 and Fig. 9, most of the X-ray selected stars lie close to or to the right of the 8–10 Myr isochrones. Taking the uncertainties of the photometry into account (~ 0.05 mag), the CMDs are consistent with the assumption that the majority of the X-ray selected low-mass stars have ages of $\sim 8 - 10$ Myr. This result is in good agreement with the above-mentioned previous age estimates for NGC 3293, which were

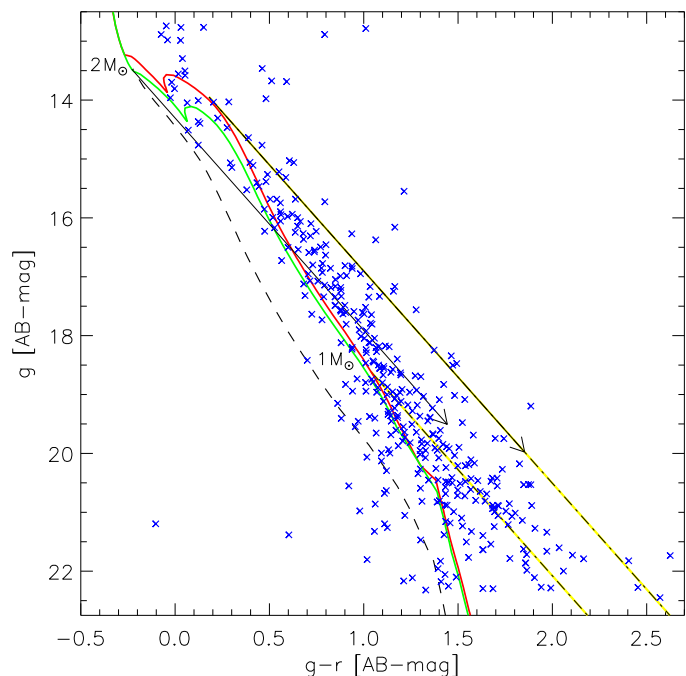
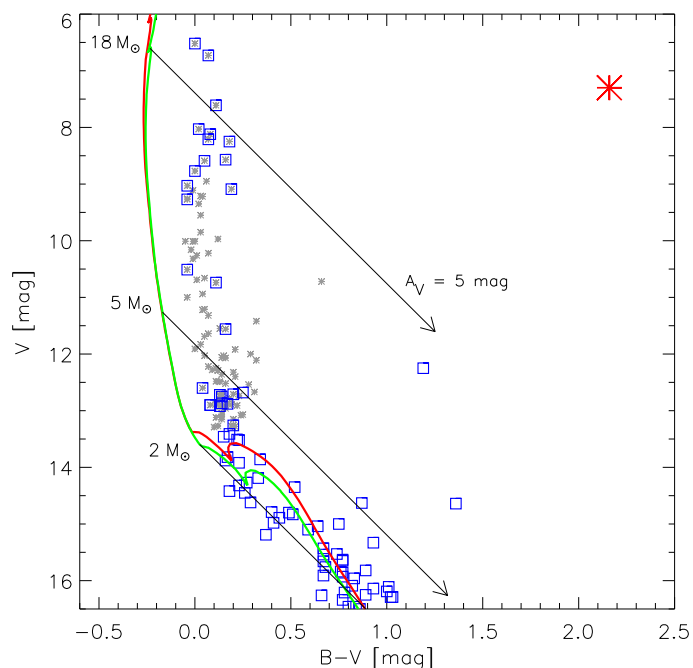


Fig. 9. Top: Optical color magnitude diagram of the X-ray detected objects in NGC 3293 based on the optical photometry from Baume et al. (2003), complemented by values from Dufton et al. (2006) for the B-type stars. The gray asterisks mark stars with known spectral type in the ACIS-I field. The X-ray sources are marked by blue squares. The solid lines in red and green show isochrones for stellar ages of 8 Myr and 10 Myr based on the PARSEC stellar models. The arrows indicate reddening vectors for $A_V = 5$ mag starting at the location of 10 Myr old stars with masses of $18 M_\odot$, $5 M_\odot$, and $2 M_\odot$. The large red star marks the M1.5Iab supergiant V361 Car.

Bottom: Optical color magnitude diagram of the X-ray detected stars in NGC 3293 based on photometry from the VST VPHAS-DR2 survey data (blue crosses). The solid lines in red and green show isochrones for stellar ages of 8 Myr and 10 Myr based on the PARSEC stellar models, and the black dashed line indicates the main sequence. The arrows show reddening vectors for $A_V = 5$ mag starting at the location of 10 Myr old stars with masses of $2 M_\odot$ and $1 M_\odot$. The yellow-and-black dot-dashed lines show the upper and lower limits for the ranges that were used to count the number of stars in the $[1 - 2] M_\odot$ interval.

based on CMD positions of the high-mass stars and the comparison with post-main-sequence evolutionary tracks. This consistency suggests a common age of about 10 Myr for the high- and the low-mass stars in NGC 3293.

4.3.4. Size of the X-ray selected stellar population of NGC 3293

Before we can quantify the population of X-ray detected young stars in NGC 3293, we first have to define the area over which we assume X-ray detected stars to be cluster members. As shown in Sect. 4.2, the stellar cluster has a radial extent of about 7 arcmin. This value for the radius is also supported by the fact that it just encloses all those 45 B-type stars for which Dufton et al. (2006) determined a stellar mass of $M \geq 5 M_{\odot}$. This circular region also contains the large majority of all X-ray sources with infrared counterparts, supporting the chosen value.

We determine the cluster population from the NIR CMD of the X-ray detected stars, since – as described above – the optical VST data are not sensitive enough to detect all the X-ray detected stars in NGC 3293. In the J versus $J - H$ diagram in Fig. 8, the number of X-ray detected stars with CMD positions that are consistent with young stellar members of NGC 3293 (i.e., at most 0.05 mag [the 1σ uncertainty of the photometry] to the left of the 10 Myr isochrone, or to the right of the 10 Myr isochrone, and above the reddening vector starting from the location of 10 Myr old $0.1 M_{\odot}$ stars) in the 7 arcmin radius region is 511. We note that the inclusion of the *Chandra* sources that have point-like counterparts in the VISTA images that are missing from the VISTA catalog and photometry with $\leq 20\%$ uncertainties would raise that number by 31, i.e., to 542.

This number can now be compared to the numbers of X-ray detected stars in the other clusters in the CNC, as listed in Table 1 of Feigelson et al. (2011). Since these other clusters were also studied with *Chandra* observations of almost identical sensitivity (see Townsley et al. 2011), a quantitative comparison is straightforward. The three most populous clusters in the central Carina Nebula are Tr 14 with 1378 X-ray detected stars, Tr 15 with 481 X-ray detected stars, and Tr 16 with 530 X-ray detected stars. This comparison shows that NGC 3293 is clearly one of the most populous clusters in the entire CNC. It is less populous than Tr 14, but almost equal to Tr 16 and Tr 15, and more populous than all the other known clusters in the CNC. NGC 3293 is thus an important part of the CNC (see discussion in Sect. 6).

4.3.5. Size of the low-mass population and the mass function of NGC 3293

New information about the mass function of the cluster can be obtained by comparing the number of X-ray detected low-mass stars in a given mass range to the known number of high-mass stars that were identified in optical spectroscopic studies. This will also provide an important clarification about the previous claims of a significant deficit of low-mass stars in NGC 3293 that were made in some optical photometric studies (Slawson et al. 2007; Delgado et al. 2011).

Our aim here is to determine the number of stars in the $[1 - 2] M_{\odot}$ mass range. To this end, we count the number of X-ray detected stars at positions in the color magnitude diagram that are consistent with masses between $1 M_{\odot}$ and $2 M_{\odot}$ for an age of 8–10 Myr; this concerns all objects with positions in a ± 0.05 mag band around the 10 Myr isochrone line for $[1 - 2] M_{\odot}$ or at locations to the right of this isochrone shifted along the

direction of the reddening vector (as indicated by the yellow-and-black lines in Fig. 8 and Fig. 9). The total number of such VISTA catalog stars in the 7 arcmin cluster region is 179 in the J versus $J - H$ diagram. In the optical g versus $g - r$ diagram, the corresponding number of VST catalog stars is 168 in the same 7 arcmin cluster region.

In order to estimate the underlying stellar population, this number of X-ray detected stars has to be corrected for the finite X-ray detection completeness, which is also a function of the location of the stars in the ACIS-I field (due to the variation of the X-ray sensitivity with off-axis angle). In order to estimate what fraction of the stars in a certain mass range can be detected at a specific local detection limit, we use here the X-ray luminosity functions of young stars derived in the context of the *Chandra* Orion Ultradeep Project (COUP) (Preibisch & Feigelson 2005). In the central part of our *Chandra* image, the weakest detected X-ray sources have X-ray luminosities of $\log(L_X[\text{erg/s}]) \approx 29.6$, if we assume a thermal plasma with $kT = 1$ keV and an absorbing column density of $N_H = 2 \times 10^{21} \text{ cm}^{-2}$ (corresponding to $A_V \approx 1$ mag). A comparison to the X-ray luminosity function of solar-mass [$0.9 M_{\odot} \leq M \leq 1.2 M_{\odot}$] stars with ages of a few Myr in Preibisch & Feigelson (2005) shows that $\approx 90\%$ of the stars will be above this limit. With an age of ≈ 8 –10 Myr, NGC 3293 is somewhat older, and the X-ray luminosities of the stars are thus expected to be slightly lower; on the other hand, stars slightly more massive than one solar mass will have somewhat higher X-ray luminosities. Therefore, assuming a completeness factor of $\approx 90\%$ is a reasonable choice for coronally active young stars in the center of NGC 3293 in the mass range $\approx [1 - 2] M_{\odot}$.

Since the cluster has a spatial extent of several arcminutes, we have to take the variation of the X-ray detection limit as a function of off-axis angle into account. For this, we use the results derived in the detailed study of Broos et al. (2011b) and summarized in their Table 8, where the variation of the X-ray luminosity limit is determined for different ranges of the off-axis angle. As listed there, the X-ray luminosity limit in the off-axis angle range $[3.8 - 6.3]$ arcmin is 0.5 dex higher than in the central 3.8 arcmin; in the $[6.3 - 7.5]$ arcmin off-axis angle range it is 0.6 dex higher than in the central 3.8 arcmin. From these numbers, we find X-ray luminosity function completeness factors of $\approx 60\%$ for stars in the off-axis angle range $[3.8 - 6.3]$ arcmin and $\approx 59\%$ for stars in the off-axis angle range $[6.3 - 7.5]$ arcmin.

Counting the X-ray detected stars in the 7 arcmin cluster region that have positions in the J versus $J - H$ diagram consistent with masses between $1 M_{\odot}$ and $2 M_{\odot}$ for an age of 8–10 Myr according to the PARSEC stellar models, we find the following numbers for the different off-axis angle ranges: in the central part ($\theta = [0 - 3.8]$ arcmin) we find 104 stars, in the $\theta = [3.8 - 6.3]$ arcmin range we find 70 stars, and in the $\theta = [6.3 - 7.5]$ arcmin range we find 5 stars. Dividing these numbers by the corresponding X-ray luminosity function completeness factors of 0.90, 0.60, and 0.59, yields a total extrapolated number of 241 stars as our final estimate for the total number of stars in the $[1 - 2] M_{\odot}$ mass range within the 7 arcmin cluster region. Considering the uncertainties in the determination of the X-ray luminosity function completeness factors, we use $N[1 - 2 M_{\odot}] \approx 241 \pm 25$ stars as the final result of this analysis.

We note that the true number is somewhat higher, since we omit here the 61 VISTA point source counterparts to *Chandra* sources that are lacking photometry in the VISTA catalog. If we include the stars from this group of counterparts that have $< 20\%$ photometric uncertainty into the counting, there will then be additional stars in the central off-axis bin, and the extrapolated total number estimate will be $N[1 - 2 M_{\odot}] \approx 252$ instead of 241.

As discussed in Sect. 3.5, we have to expect between about five and nine random false matches to sufficiently bright VISTA catalog sources that might be located in our counting region for the $[1-2] M_{\odot}$ stars in the CMD. These estimated false matches have to be subtracted from our estimate of the stellar population. However, we should also note that six of the ten above-mentioned VISTA sources missing from the VISTA catalog that correspond to X-ray detected stars in the $[1-2] M_{\odot}$ range, have an optical counterpart in the VST VPHAS-DR2 point source catalog. At least these six additional VISTA stars should thus certainly be included into the counts. The difference between the five to nine objects that should be subtracted and the six objects that should be added is small compared to the above given uncertainty range ± 25 . Therefore, we conclude that our result of $N[1-2 M_{\odot}] \approx 241 \pm 25$ is robust.

This number can now be compared to the size of the high-mass population in the same $R = 7'$ region. In addition to the above-mentioned 45 B-type stars with listed masses between $5 M_{\odot}$ and $40 M_{\odot}$ (Dufton et al. 2006), the red supergiant V361 Car is also located in this region. The total number of high-mass stars in this cluster region is thus 46. Using the numerical representation of the canonical field star IMF from Kroupa (2002) and the number of 46 stars in the $[5-40] M_{\odot}$ range, the expected number of $[1-2] M_{\odot}$ stars is $N_{\text{IMF exp}} = 237$. The X-ray completeness-corrected number of $N[1-2 M_{\odot}] \approx 241 \pm 25$ such stars (253 ± 25 , if the stars missing in the VISTA catalog are included) derived above is in very good agreement with this expectation value.

This good agreement suggests that the size of the solar-mass population of NGC 3293 is consistent with the expectations from the normal field star IMF. This result refutes earlier claims for a strong deficit of stars with mass below $M \leq 2-3 M_{\odot}$. This highlights the difficulties resulting in purely photometric determinations of cluster populations, especially in regions with a very strong galactic background such as in NGC 3293.

We cannot directly determine the IMF in the subsolar and very low-mass range with our data since the X-ray detected sample is very incomplete at such low stellar masses. Assuming that the IMF of NGC 3293 follows the field IMF down to $0.1 M_{\odot}$, a numerical extrapolation (based again on the 46 high-mass stars) of the field star IMF suggests 3230 stars in the $[0.1-1] M_{\odot}$ range. In the same way, an estimate of the total stellar population of 3625 stars in the $[0.1-100] M_{\odot}$ range can be computed.

The statistical expectation value of the number of very high-mass stars (above $40 M_{\odot}$) is 2.3. The central 68% Poisson range is $[1-4]$ such stars, which should have already exploded as supernovae.

5. X-ray properties of the B-type stars

The large number of B-type stars in NGC 3293 provides a good opportunity to investigate the X-ray properties in a co-eval and homogeneous population of B-type stars, covering the full spectral range from B0 to B9.

It is well established that most of the hottest B-type stars (spectral types B0 to \approx B2) are rather strong X-ray sources; their X-ray emission is thought to be related to their strong stellar winds, similar to the case of O-type stars (e.g., Zhekov & Palla 2007; Cohen et al. 2014). Most B-type stars with spectral types later than \approx B2 remain undetected in X-ray observations; this is in good agreement with the theoretical expectations, since these stars only have relatively weak winds that are incapable of producing strong X-ray emission, and at the same time the B-type stars (and also the A-type stars) have no outer convection zones,

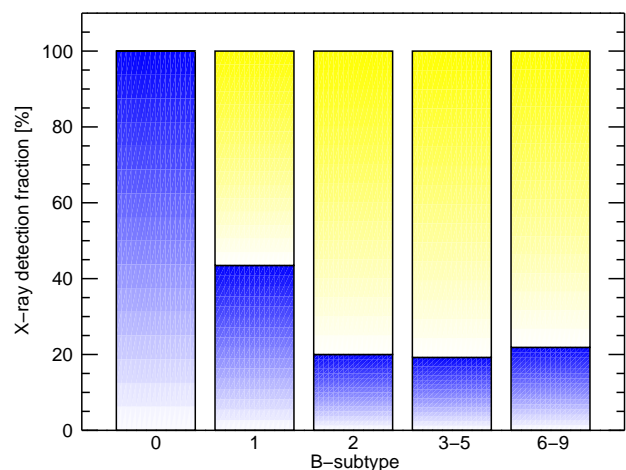


Fig. 10. Fraction of X-ray detections (blue shaded histogram) as a function of spectral type.

and thus no magnetic dynamo action is expected, which is the prerequisite for the X-ray emission due to coronal magnetic activity (as in the late-type stars).

Nevertheless, in many young clusters, a significant fraction of late B-type stars shows detectable amounts of X-ray emission (e.g., Stelzer et al. 2005; Gagné et al. 2011). An often invoked explanation is the presence of unresolved late-type companions as the true source of the X-rays. The X-ray properties of these late B-type stars will then contain information about the multiplicity and the nature of their low-mass companion stars.

5.1. X-ray detection fraction as a function of spectral type

In the full sample of 97 B-type stars in the ACIS-I field, 24 are detected as X-ray sources. The detection fraction, however, is a strong function of spectral type, as shown in Fig. 10. While all (three) B0 stars are detected, the fraction drops to $10/23 \approx 43\%$ for the B1 stars, and then to $\approx 20\%$ for later B spectral types.

If we assume that for all of these X-ray detected later B-type stars the X-ray emission originates from an unresolved late-type companion, information about the multiplicity and the pairing-statistics of these B-type stars can be inferred. Since X-ray luminosity scales with stellar mass, these companions cannot have stellar masses that are too low; a reasonable guess is that these companions should be stars with $M \gtrsim 1 M_{\odot}$ in order to produce X-ray luminosities above our detection limits.

If we assume that every B-type star has one companion (i.e., a multiplicity of 100%), and further assume that the companion masses are randomly sampled from the conventional field-star IMF, it can easily be calculated that the expected fraction of B-type stars with companions of mass $\geq 1 M_{\odot}$ would be $\approx 6.8\%$. This value is lower than the observed X-ray detection rate of $\approx 20\%$ and thus implies that either these B-type stars have more than one companion on average or that the companion masses are not established by random sampling, but are biased towards more massive stars. This supports independent observational results which also suggest a very high multiplicity of intermediate- to high-mass stars (see, e.g., Preibisch et al. 1999; Duchêne & Kraus 2013) and mass ratios that are higher than expected from random pairing. Our result also agrees with

⁷ According to the Kroupa (2002) IMF, the ratio of stars in the $[1-2] M_{\odot}$ range to those in the $[0.1-2] M_{\odot}$ range is 0.068.

previous findings based on X-ray observations of other young clusters (see, e.g., Evans et al. 2011).

5.2. X-ray properties of the individual B-type stars

For a more quantitative analysis, we determined the X-ray properties of the individual B-type stars. For those four B-type stars with a sufficient number of X-ray counts, spectral fitting was performed with XSPEC. In the other cases, we used the conversion factor from counts to unabsorbed flux as determined by `srcflux`, employing the optically derived individual extinction of each star to fix the hydrogen column density, and assuming a plasma temperature of $kT = 0.5$ keV for these stars. The `srcflux` tool was also used for those B-stars without an X-ray counterpart in our source list, in order to compute 90% upper limits to their count rates and X-ray luminosities.

In the following, we briefly discuss the individual X-ray properties of some of the X-ray detected B-type stars. The full set of information about the X-ray luminosities (or the corresponding upper limits) for the B-type stars is contained in the electronic Table 3, available at the CDS.

HD 91969:

The optically brightest ($V = 6.51$) cluster member is the B0 Ib star HD 91969, for which a stellar mass of $M \approx 40 M_{\odot}$ has been estimated (Dufton et al. 2006). HD 91969 provides a perfect match to the *Chandra* source 542, which yielded 164.4 net counts and shows a rather soft spectrum with a median photon energy of 1.0 keV. The XSPEC fit with a thermal plasma model and the N_{H} parameter fixed to the value $0.136 \times 10^{22} \text{ cm}^{-2}$ (as determined from the optical color excess) yields a plasma temperature of $T \approx 5.7 \pm 1.1$ MK. This is within the typical range of plasma temperatures of early B-type stars, for which the X-ray emission is assumed to originate from shocks in the fast stellar wind (Stelzer et al. 2005). Since the fit is of mediocre quality ($\chi^2/\nu = 2.92$), we also tried models with two plasma components; however, they yielded no improvement to the fit quality. The X-ray luminosity of the best-fit model is $L_{\text{X}} = 2.78 \times 10^{31} \text{ erg/sec}$ and yields a fractional X-ray luminosity of $L_{\text{X}}/L_{\text{bol}} = 3.0 \times 10^{-8}$, close to the typical ratios found for early B-type stars.

We note that two further (but much weaker) X-ray sources were detected very close to HD 91969: source 537, located $1.4''$ to the west of HD 91969 with 4.2 net counts, and source 548, located $3.0''$ to the northeast of HD 91969 with 6.9 net counts. In the available optical and NIR images, no indication of the presence of stars is seen at these locations because the source positions are within the very bright (or even saturated) parts of the PSF of the extremely bright star HD 91969. It therefore remains unclear, whether these two X-ray sources might be (presumably late-type) companions to HD 91969.

HD 91943:

The optically second brightest ($V = 6.69$) star, HD 91943, has a spectral type B0.7 Ib and an estimated stellar mass of $M \approx 30 M_{\odot}$. This star provides a perfect match to the X-ray source 418, which yielded 38.8 net counts with a median energy of 1.1 keV. The fit to the X-ray spectrum yielded a plasma temperature of $T = 8.5 \pm 4.6$ MK and an X-ray luminosity of $L_{\text{X}} = 4.1 \times 10^{30} \text{ erg/sec}$. This corresponds to a fractional X-ray luminosity of $L_{\text{X}}/L_{\text{bol}} \approx 7 \times 10^{-9}$.

No further X-ray source is detected within $8''$ of HD 91943.

CPD –57°3524A:

This B0.5 III star is a good match to *Chandra* source 704; with

20.8 net counts, the X-ray source is too weak for a spectral fitting analysis, but the relatively low median energy of 1.3 keV is in the typical range for B-type stars (see Fig. 4 in Gagné et al. 2011).

CPD –57°3526B:

This B1 III star is a very good match to *Chandra* source 710, which has 4.6 net count and a median energy of 1.3 keV. Although the X-ray detection is unquestionable, the X-ray properties remain somewhat unclear because the source detection revealed another, similarly strong source with number 709 (3.5 net counts, $E_{\text{med}} = 0.8$ keV) at an angular distance of just $0.68''$ from source 710.

Unfortunately, in all the available optical and infrared images of this very bright star ($V = 8.25$, $H = 8.03$) the inner few square arcseconds of the PSF are completely saturated; it is therefore not possible to check whether the second X-ray source is a companion to the B1 star.

CD –57°3348:

The B1 III star CD –57°3348 (alias CPD –57°3506A) is a very good match to *Chandra* source 490, which yielded 42.8 net counts with a median energy of 1.0 keV. The fit to the X-ray spectrum yielded a plasma temperature of $T = 7.9 \pm 4.5$ MK and an X-ray luminosity of $L_{\text{X}} = 5.4 \times 10^{30} \text{ erg/sec}$. This corresponds to $L_{\text{X}}/L_{\text{bol}} \approx 2.3 \times 10^{-8}$.

We note that the VISTA images show another fainter star $3''$ to the north of this B1 III star, which is also detected as an X-ray source. Since these $3''$ correspond to a physical distance of about 7000 AU, it remains unclear whether this fainter star might be a companion to the B1 III star, or just a random projection effect.

CPD –57°3523:

This B1 III star is a very good match to *Chandra* source 697. With 14.8 net counts the X-ray source is too weak for spectral fitting, but the median energy of 0.9 keV is in the typical range for early B-type stars.

V405 Car:

The B1 V star V405 Car (alias CPD –57°3507) is a very good match to *Chandra* source 523, which has 3.8 net counts and $E_{\text{med}} = 2.7$ keV; this is unusually hard for a B star and thus indicates that a low-mass companion contributes to the observed X-ray emission.

CPD –57°3521:

The B1 III star CPD –57°3521 is a very good match to *Chandra* source 679, which has 14.7 net counts and $E_{\text{med}} = 1.4$ keV.

The X-ray analysis revealed another, weaker (2.8 net counts) but somewhat harder ($E_{\text{med}} = 2.0$ keV) X-ray source (680) at an angular distance of just $0.82''$ from source 679. Unfortunately, the reality of this tentative (late-type?) companion cannot be checked since in all available optical and infrared images of this very bright star ($V = 8.14$, $H = 7.87$) the inner few square arcseconds of the PSF are completely saturated.

NGC 3293 ESL 87:

The B5 star NGC 3293 ESL 87 is a good match to *Chandra* source 47, which has 25.9 net counts and $E_{\text{med}} = 1.6$ keV. The XSPEC fit to the X-ray spectrum (with N_{H} fixed at $0.1 \times 10^{22} \text{ cm}^{-2}$) yields a plasma temperature of $kT = 2.1 \pm 1.5$ keV and an X-ray luminosity of $4.6 \times 10^{30} \text{ erg/sec}$. These values would be very unusual for a B5 star and thus point towards the presence of a late-type companion.

Other B-type stars in NGC 3293:

Most of the other B-type stars in the ACIS-I field are not detected as X-ray sources. As described above, we use the `srcflux` tool

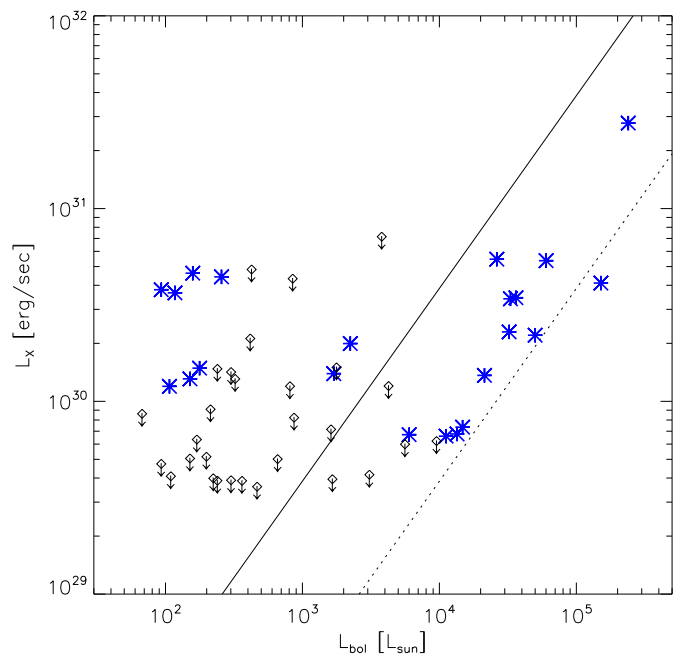


Fig. 11. X-ray versus bolometric luminosity of the known B-type stars in NGC 3293. The blue asterisks show the X-ray detected stars. Upper limits for the non-detected B-type stars are marked with the small diamonds with downward-pointing arrows. The solid line marks the relation $L_X/L_{\text{bol}} = 10^{-7}$, the dotted line $L_X/L_{\text{bol}} = 10^{-8}$.

to determine 90% upper limits to the X-ray luminosities of the undetected B-type stars. This yielded useful upper limits for 31 of the undetected B-type stars; for the remaining targets, *srcflux* could not determine upper limits because they are located very close to a chip edge on the detector. The upper limit values determined in this way reflect the local X-ray detection limit at the target position. The three B-type stars with particularly high ($\geq 2 \times 10^{30}$ erg/s) upper limits (see Fig. 11) are located very close to the edge of the ACIS-I detector where the sensitivity is considerably lower than on-axis.

5.3. X-ray and bolometric luminosity

In Fig. 11 we plot the X-ray luminosities of the detected B-type stars (and the upper limits to the X-ray luminosities of the undetected B-type stars) against the bolometric luminosities.

Most of the very luminous objects ($L_{\text{bol}} \gtrsim 10^4 L_{\odot}$) show fractional X-ray luminosities between $L_X/L_{\text{bol}} = 10^{-7}$ and $L_X/L_{\text{bol}} \approx 10^{-8}$. This is the typical range found for early B-type stars in other young clusters (e.g., Stelzer et al. 2005; Gagné et al. 2011) and is consistent with the wind-shock model for the origin of the X-ray emission.

The X-ray detected later B-type stars show considerably higher L_X/L_{bol} ratios, which would be very hard to explain by the wind-shock mechanism thought to be at work in the early B-type stars. Their X-ray luminosities are, however, consistent with those of young late-type stars, again strongly suggesting that the X-ray emission actually originates from unresolved late-type companion stars.

5.4. Red supergiant star V361 Car (M1.5Iab-Ib)

In order to describe all known massive stars in NGC 3293, we note that the red supergiant star V361 Car (M1.5Iab-Ib) (which

is the most massive star in the cluster) is not detected as an X-ray source.

However, the X-ray source 449 is found just 2.8 arcsec south-east of V361 Car. With 4.9 net counts and a relatively soft spectrum ($E_{\text{med}} = 1.2$ keV), this might be either a late-type companion, or an early B-star companion to V361 Car. Owing to the extreme brightness of the supergiant ($V = 7.19$, $H = 2.6$), all available optical and infrared images are completely saturated at the position of this possible companion.

6. Summary and conclusions

We have performed the first deep X-ray observation of the young cluster NGC 3293 at the northwestern edge of the Carina Nebula Complex. This *Chandra* observation complements the similarly sensitive X-ray survey of the central region of the CNC in the context of the CCCP (Townsend et al. 2011) and our recent observation of the NGC 3324 region (between the central parts of the CNC and NGC 3293), and it completes the X-ray investigation of all the star clusters in the CNC. The present study is the first where NGC 3293 is investigated in the same way as all other clusters in the CNC (i.e., by a combination of a deep X-ray and infrared data). This finally allows us to put the derived properties of NGC 3292 into a larger context and to consider it in the same way as the other parts of the CNC.

Our analysis of the *Chandra* X-ray observation of NGC 3293 clearly shows that the cluster hosts a large population of low-mass stars in the $\sim [2 - 0.5] M_{\odot}$ mass range. The number of X-ray detected low-mass stars closely agrees with the expectations based on the number of spectroscopically identified high-mass stars and the assumption of a field star initial mass function. There is thus no indication of a deficit of low-mass ($M \leq 2.5 M_{\odot}$) stars in this cluster. These results suggest a total population of ≈ 3600 stars for NGC 3293.

We find that NGC 3293 is one of the most populous clusters in the entire Carina Nebula Complex. NGC 3293 is older than the other well-investigated clusters in the CNC. Extrapolating the cluster's mass function suggests that several supernova explosions have occurred in NGC 3293 during the last few Myr (see also Voss et al. 2012). This suggests that NGC 3293 has most likely played an important role during the formation and early evolution of the CNC.

With a spatial extent of ~ 100 pc, a total cloud mass of $\sim 10^6 M_{\odot}$, and more than 100 000 young stars, the CNC is one of the largest star forming complexes in our galaxy. It also shows a high diversity in the structure of the clouds and in the spatial configurations of the stellar populations. Most of the stars in the inner parts of the CNC are located in one of more than ten individual stellar clusters, which have ages ranging from $\lesssim 1$ Myr up to ~ 5 Myr. In addition to this clustered stellar population, there is also an unclustered, widely distributed population (see Feigelson et al. 2011) of young stars with ages ranging from < 1 Myr to $\sim 6 - 8$ Myr (Preibisch et al. 2011a). How this complicated and diverse spatial and temporal configuration has formed and evolved is still unclear.

In Fig. 12 we show a sketch illustrating the spatial configuration of the most significant clusters and clouds in the CNC. NGC 3293 is the oldest of the large clusters in the CNC, and it is located at the northwestern edge of the complex. Most of the current star formation activity observed today in the CNC is happening in the southeastern part of the CNC, in the Southern Pillars region, i.e., at the opposite end of the complex. However, this does not reflect a systematic northwest to southeast spatial

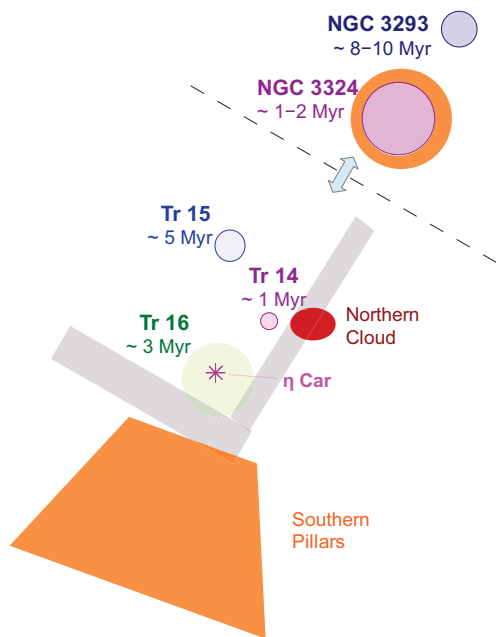


Fig. 12. Sketch illustrating the locations and orientations of the main clusters and clouds in the Carina Nebula Complex. The circles indicate the locations and the approximate sizes of the individual stellar clusters. The orange and red structures indicate the approximate extent of the densest clouds, and the gray rectangles mark the V-shaped lane of dark clouds intersecting the central parts of the Carina Nebula. As indicated by the dashed line and the double arrow, the distance of NGC 3324 and NGC 3293 from the center of the Carina Nebula is actually somewhat greater than in this sketch.

age gradient since there are several sites of active star formation in the northern part of the complex. The most prominent of these is the large shell of dense dust clouds around the cluster NGC 3324 (see Ohlendorf et al. 2013), which is located just southeast of NGC 3293. Another example of very recent and ongoing star formation activity in the northern area is the embedded stellar cluster associated with the massive dense cloud clump G286.21+0.17 (see Ohlendorf et al. 2013), which is located north of the dust shell around NGC 3324.

The cluster ages also show no systematic trend with spatial position in the complex. For example, the very young ($\sim 1 - 2$ Myr) cluster NGC 3324 is located between the considerably older clusters NGC 3293 ($\sim 8 - 10$ Myr) to the north and the ~ 5 Myr old cluster Tr 15 south of it.

Instead of a systematic progression of star formation in one direction, it appears that the star formation activity in the CNC was “wandering around” in various directions that changed with time. The best explanation of this seems to be that the progression of star formation in the CNC was predominantly triggered by the feedback of the numerous high-mass stars that were born at different locations in the complex over the last ~ 10 Myr.

Today, we witness the effect of this feedback and the corresponding driving of star formation everywhere in the surroundings of the currently existing O-type stars. For example, the ~ 3 Myr high-mass stars in the cluster Tr 16 are triggering star formation in the Southern Pillars (see Smith et al. 2010b; Povich et al. 2011). The very young (~ 1 Myr) high-mass stars in the cluster Tr 14 have recently started to exert a strong influence on the very dense and massive cloud (known as the Northern Cloud; see Brooks et al. 2003; Kramer et al. 2008; Preibisch et al. 2011c,b) to the west of the stellar cluster; in the near future,

the ongoing compression of this cloud is likely to initiate cloud collapse and trigger star formation. The young ($\sim 1 - 2$ Myr) O-type stars in the cluster NGC 3324 (Preibisch et al. 2014a) have swept up a huge dust bubble around the Gum 31 HII region and are starting to trigger star formation in and around this bubble (Ohlendorf et al. 2013).

About 8 Myr ago, the (then very young) cluster NGC 3293 probably contained several O-type stars. These high-mass stars must have exerted a similar influence on the clouds that were present in the cluster’s surroundings at that time. It appears likely that this stellar feedback initiated the sequence of local cloud collapse events in the original, huge proto-Carina Nebula cloud, starting probably at the location where we now find the second oldest cluster Tr 15. Given the age difference of $\sim 3 - 5$ Myr between NGC 3293 and Tr 15, it seems possible that supernova explosions of the O-type stars may have played an important role in the timing of the propagating star formation.

Today, i.e., about 8–10 Myr later, star formation is still going on in some locations of the complex. Although a large fraction of the original $\sim 10^6 M_{\odot}$ gas has already been heated and transformed to lower densities by the effects of the radiation, winds, and supernovae of several generations of massive stars (Preibisch et al. 2012), there is still a large reservoir ($\gtrsim 20\,000 M_{\odot}$) of dense clouds (see Preibisch et al. 2011c) available for future star formation over the next millions of years.

These considerations show that a good characterization of the ages and stellar populations of clusters like NGC 3293 is a key factor for understanding the intricate spatio-temporal progression of star formation in huge cloud complexes like the CNC.

Acknowledgements. We gratefully acknowledge funding for this project by the German *Deutsche Forschungsgemeinschaft*, DFG project number PR 569/9-1. Additional support came from funds from the Munich Cluster of Excellence: “Origin and Structure of the Universe”. Townsley and Broos acknowledge support from the *Chandra X-ray Observatory* general observer grant GO5-16003X and from the Penn State ACIS Instrument Team Contract SV4-74018, issued by the *Chandra X-ray Center* (CXC), which is operated by the Smithsonian Astrophysical Observatory for and on behalf of NASA under contract NAS8-03060. This research used software provided by the CXC in the application package *CIAO*, and *SAOImage DS9* software developed by the Smithsonian Astrophysical Observatory. The VISTA infrared data used in this work are based on observations made with ESO Telescopes at the La Silla Paranal Observatory under programme ID 088.C-0117. The analysis used data products from observations made with ESO Telescopes at the La Silla Paranal Observatory under program ID 177.D-3023, as part of the VST Photometric $H\alpha$ Survey of the Southern Galactic Plane and Bulge (VPHAS+, www.vphas.eu). We acknowledge the assistance of the LMU physics students S. GraBl, J. Diehl, and L. Furtak in some steps of the preliminary data analysis. This research has made use of the SIMBAD database and the VizieR catalog services operated at Strasbourg astronomical Data Center (CDS).

References

- Anders, E. & Grevesse, N. 1989, *Geochim. Cosmochim. Acta*, 53, 197
 Baume, G., Vázquez, R. A., Carraro, G., & Feinstein, A. 2003, *A&A*, 402, 549
 Brooks, K. J., Cox, P., Schneider, N., et al. 2003, *A&A*, 412, 751
 Broos, P., Townsley, L., Getman, K., & Bauer, F. 2012, *AE: ACIS Extract, Astrophysics Source Code Library*
 Broos, P. S., Getman, K. V., Povich, M. S., et al. 2011a, *ApJS*, 194, 4
 Broos, P. S., Townsley, L. K., Feigelson, E. D., et al. 2010, *ApJ*, 714, 1582
 Broos, P. S., Townsley, L. K., Feigelson, E. D., et al. 2011b, *ApJS*, 194, 2
 Cohen, D. H., Li, Z., Gayley, K. G., et al. 2014, *MNRAS*, 444, 3729
 Davis, J. E., Bautz, M. W., Dewey, D., et al. 2012, in *Proc. SPIE*, Vol. 8443, Space Telescopes and Instrumentation 2012: Ultraviolet to Gamma Ray, 84431A
 Delgado, A. J., Alfaro, E. J., & Yun, J. L. 2011, *A&A*, 531, A141
 Della Ceca, R., Carrera, F. J., Caccianiga, A., et al. 2015, *MNRAS*, 447, 3227
 Dias, W. S., Alessi, B. S., Moitinho, A., & Lépine, J. R. D. 2002, *A&A*, 389, 871
 Drew, J. E., Gonzalez-Solares, E., Greimel, R., et al. 2014, *MNRAS*, 440, 2036

- Duchêne, G. & Kraus, A. 2013, *ARA&A*, 51, 269
- Dufton, P. L., Smartt, S. J., Lee, J. K., et al. 2006, *A&A*, 457, 265
- Evans, C. J., Smartt, S. J., Lee, J.-K., et al. 2005, *A&A*, 437, 467
- Evans, N. R., DeGioia-Eastwood, K., Gagné, M., et al. 2011, *ApJS*, 194, 13
- Fedele, D., van den Ancker, M. E., Henning, T., Jayawardhana, R., & Oliveira, J. M. 2010, *A&A*, 510, A72
- Feigelson, E., Townsley, L., Güdel, M., & Stassun, K. 2007, *Protostars and Planets V*, 313
- Feigelson, E. D., Getman, K. V., Townsley, L. K., et al. 2011, *ApJS*, 194, 9
- Feigelson, E. D., Townsley, L. K., Broos, P. S., et al. 2013, *ApJS*, 209, 26
- Fruscione, A., McDowell, J. C., Allen, G. E., et al. 2006, in *Proc. SPIE*, Vol. 6270, Society of Photo-Optical Instrumentation Engineers (SPIE) Conference Series, 62701V
- Gagné, M., Fehon, G., Savoy, M. R., et al. 2011, *ApJS*, 194, 5
- Garmire, G. P., Bautz, M. W., Ford, P. G., Nousek, J. A., & Ricker, Jr., G. R. 2003, in *Proc. SPIE*, Vol. 4851, X-Ray and Gamma-Ray Telescopes and Instruments for Astronomy., ed. J. E. Truemper & H. D. Tananbaum, 28–44
- Güdel, M., Briggs, K. R., Arzner, K., et al. 2007, *A&A*, 468, 353
- Kharchenko, N. V., Piskunov, A. E., Röser, S., Schilbach, E., & Scholz, R.-D. 2005, *A&A*, 438, 1163
- Kramer, C., Cubick, M., Röllig, M., et al. 2008, *A&A*, 477, 547
- Kroupa, P. 2002, *Science*, 295, 82
- Kuijken, K. 2011, *The Messenger*, 146, 8
- Lehmer, B. D., Xue, Y. Q., Brandt, W. N., et al. 2012, *ApJ*, 752, 46
- Lucy, L. B. 1974, *AJ*, 79, 745
- Marigo, P., Girardi, L., Bressan, A., et al. 2017, *ApJ*, 835, 77
- McLeod, A. F., Gritschneider, M., Dale, J. E., et al. 2016, *MNRAS*, 462, 3537
- Ohlendorf, H., Preibisch, T., Gaczkowski, B., et al. 2013, *A&A*, 552, A14
- Povich, M. S., Smith, N., Majewski, S. R., et al. 2011, *ApJS*, 194, 14
- Preibisch, T., Balega, Y., Hofmann, K.-H., Weigelt, G., & Zinnecker, H. 1999, *New A*, 4, 531
- Preibisch, T. & Feigelson, E. D. 2005, *ApJS*, 160, 390
- Preibisch, T., Hodgkin, S., Irwin, M., et al. 2011a, *ApJS*, 194, 10
- Preibisch, T., Kim, Y.-C., Favata, F., et al. 2005, *ApJS*, 160, 401
- Preibisch, T., Mehlhorn, M., Townsley, L., Broos, P., & Ratzka, T. 2014a, *A&A*, 564, A120
- Preibisch, T., Ratzka, T., Kuderna, B., et al. 2011b, *A&A*, 530, A34
- Preibisch, T., Roccatagliata, V., Gaczkowski, B., & Ratzka, T. 2012, *A&A*, 541, A132
- Preibisch, T., Schuller, F., Ohlendorf, H., et al. 2011c, *A&A*, 525, A92
- Preibisch, T., Zeidler, P., Ratzka, T., Roccatagliata, V., & Petr-Gotzens, M. G. 2014b, *A&A*, 572, A116
- Schuller, F., Menten, K. M., Contreras, Y., et al. 2009, *A&A*, 504, 415
- Siess, L., Dufour, E., & Forestini, M. 2000, *A&A*, 358, 593
- Slawson, R. W., Ninkov, Z., & Horch, E. P. 2007, *Ap&SS*, 312, 171
- Smith, N. 2006, *MNRAS*, 367, 763
- Smith, N., Bally, J., & Walborn, N. R. 2010a, *MNRAS*, 405, 1153
- Smith, N. & Brooks, K. J. 2008, *The Carina Nebula: A Laboratory for Feedback and Triggered Star Formation*, ed. B. Reipurth, 138
- Smith, N., Povich, M. S., Whitney, B. A., et al. 2010b, *MNRAS*, 406, 952
- Stassun, K. G., van den Berg, M., Feigelson, E., & Flaccomio, E. 2006, *ApJ*, 649, 914
- Stelzer, B., Flaccomio, E., Montmerle, T., et al. 2005, *ApJS*, 160, 557
- Townsley, L. K., Broos, P. S., Corcoran, M. F., et al. 2011, *ApJS*, 194, 1
- Voss, R., Martin, P., Diehl, R., et al. 2012, *A&A*, 539, A66
- Wang, J., Feigelson, E. D., Townsley, L. K., et al. 2011, *ApJS*, 194, 11
- Weisskopf, M. C., Brinkman, B., Canizares, C., et al. 2002, *PASP*, 114, 1
- Wolk, S. J., Broos, P. S., Getman, K. V., et al. 2011, *ApJS*, 194, 12
- Wolk, S. J., Harnden, Jr., F. R., Flaccomio, E., et al. 2005, *ApJS*, 160, 423
- Zeidler, P., Preibisch, T., Ratzka, T., Roccatagliata, V., & Petr-Gotzens, M. G. 2016, *A&A*, 585, A49
- Zhekov, S. A. & Palla, F. 2007, *MNRAS*, 382, 1124

Appendix A: Cloud structure and extinction in and around NGC 3293

NGC 3293 is located at the northwestern edge of the cloud complex associated with the Carina Nebula. The inner parts of this cloud complex host some very dense clouds, which cause very strong extinction of $A_V \gtrsim 10$ mag (see cloud column density map in Preibisch et al. 2012) at some locations. The properties and the highly inhomogeneous spatial structure of these dense clouds have been revealed by APEX sub-mm observations (Preibisch et al. 2011c).

In the NGC 3293 area, the APEX / LABOCA maps from the ATLASGAL survey (Schuller et al. 2009) show no significant sub-mm emission. Although this implies that no very dense clouds are present, *Spitzer* mid-infrared and *Herschel* far-infrared maps (see Fig. A.1) nevertheless show significant emission from moderate-density clouds in and around NGC 3293. The diffuse $24\ \mu\text{m}$ emission that is seen mainly towards the northwest of the cluster center, results most likely from warm dust grains that are heated by the UV radiation of the B-type stars in the cluster. The $8\ \mu\text{m}$ emission traces the surface of somewhat denser cloud structures; it is probably dominated by fluorescent emission from polycyclic aromatic hydrocarbon (PAH) molecules. In the southeastern part of the cluster, the *Spitzer* and *Herschel* maps show a prominent pillar-shaped cloud, which points directly towards the M1.5lab supergiant V361 Car (the very bright point source in the *Spitzer* image). This pillar is very similar to the numerous cloud pillars found in other parts of the CNC (see Smith et al. 2010b; McLeod et al. 2016).

The infrared images show a tendency of stronger cloud emission around the stellar cluster, and less emission in the central parts of the cluster. Together with the apparently empty bubble-like feature just east of the cluster center, this suggests that the radiation and winds of the high-mass stars in NGC 3293 have cleared the central regions of the original clouds. This conclusion is supported by the measured reddening values of stars with known spectral type in the NGC 3293 region listed in Dufton et al. (2006); these values correspond⁸ to typical extinction values of $A_V \sim 1$ mag for stars near the cluster center, whereas stars at the periphery show extinctions up to a few magnitudes.

Appendix B: Random matching simulation

In order to estimate the possible occurrence rate of false positive matches between a random (spurious) X-ray source and an unrelated infrared source, we performed a set of matching simulations. We take into account that neither the distribution of the infrared sources, nor the distribution and the properties of the X-ray matching regions are purely random, but rather show characteristic spatial trends.

The distribution of the infrared sources in the field is not uniform since we are looking at a stellar cluster with a higher density of relatively bright stars in the center, superposed on an approximately uniform distribution of relatively faint background objects, and a reduced sensitivity for very faint objects in the central regions around the very bright stars.

There are several reasons why the properties of the X-ray matching regions in a *Chandra* observation are also not uniform over the observed field of view. First, the sensitivity (and thus the detection limit) depends on the off-axis angle. Second, the

position uncertainties (and the corresponding radii of the matching regions) also depend on the off-axis angle since the point spread function increases with off-axis angle. Third, the position uncertainties also depend on the number of detected counts per source, which again depends on the local sensitivity (known as the effective area) at the source position on the detector. All the mentioned dependencies are, to first order, predominantly functions of the angular distance from either the cluster center or the focal point of the X-ray image; these two points coincide closely in our observation.

We therefore use the original VISTA catalog for the random matching simulations, which preserves the spatial distributions of the infrared sources. To simulate X-ray source lists, we use our original *Chandra* ACIS-I source catalog in order to conserve the angular-dependence of the source properties, but rotate all source positions by certain angles around the focal point in order to break the physical connection between X-ray and infrared sources. Simulations were performed with different rotation angles from -180° to $+180^\circ$ in steps of 0.5° . At each rotation angle, we used `match_xy` in the same way as for the original matching and recorded the number of resulting matches with the VISTA catalog. For any rotation angle that differs by more than a few degrees from zero, the resulting match numbers are a measure of the expected number of purely random matches of sources without any physical connection.

The results of these simulations are shown in Fig. B.1. For rotation angles of more than a few degrees, it can be seen that the number of matches shows only small fluctuations, and no significant variations or trends with rotation angle, confirming that the resulting numbers are good estimates of the random false match fraction.

Considering the full VISTA catalog, the mean number of random matches is 238 ± 12 ; this corresponds to a fraction of $(23.3 \pm 1.2)\%$ of all X-ray sources.

Two important aspects have to be considered in the interpretation of this number. First, it should be noted that this number is a strict upper limit to the actual number of possible random false matches in our sample since the simulation assumes (by means of the rotation) that no X-ray source is physically connected to any infrared source; it is valid only for X-ray sources that have no physical match detected in the available optical/infrared images. In reality, however, a large fraction of the X-ray sources are young stars, i.e., rather bright IR sources, that produce correct positive matches. Only those X-ray sources that have no true counterpart in the VISTA images can get a false random match.

The second point concerns the magnitudes of these random false matches. The large majority of these are very faint infrared sources, most of them with magnitudes $J > 18$. This is just a reflection of the strongly increasing number of infrared sources when going towards fainter magnitudes. The color magnitude diagrams resulting from these random matching experiments are therefore very different from the actual color magnitude diagram, since they show only very few random false matches to stars with sufficiently bright magnitudes to be considered as $\gtrsim 1 M_\odot$ stars.

To investigate this last point further, we repeated the simulations with restricted versions of the original VISTA catalog, containing only objects above a specific magnitude limit. The number of false matches drops steeply with increasing magnitude limit: for $J < 18$ we find 84 ± 9 matches ($8.2 \pm 0.9\%$), for $J < 17$ we find 47 ± 7 matches ($4.6 \pm 0.7\%$), and for $J < 16$ we find 25 ± 5 matches ($2.3 \pm 0.5\%$). This implies that the fraction of potential false matches of X-ray sources with stars that

⁸ In their optical photometric study, Baume et al. (2003) found that the extinction law for the stars in NGC 3293 is consistent with the usual relation $A_V = 3.1 E(B - V)$.

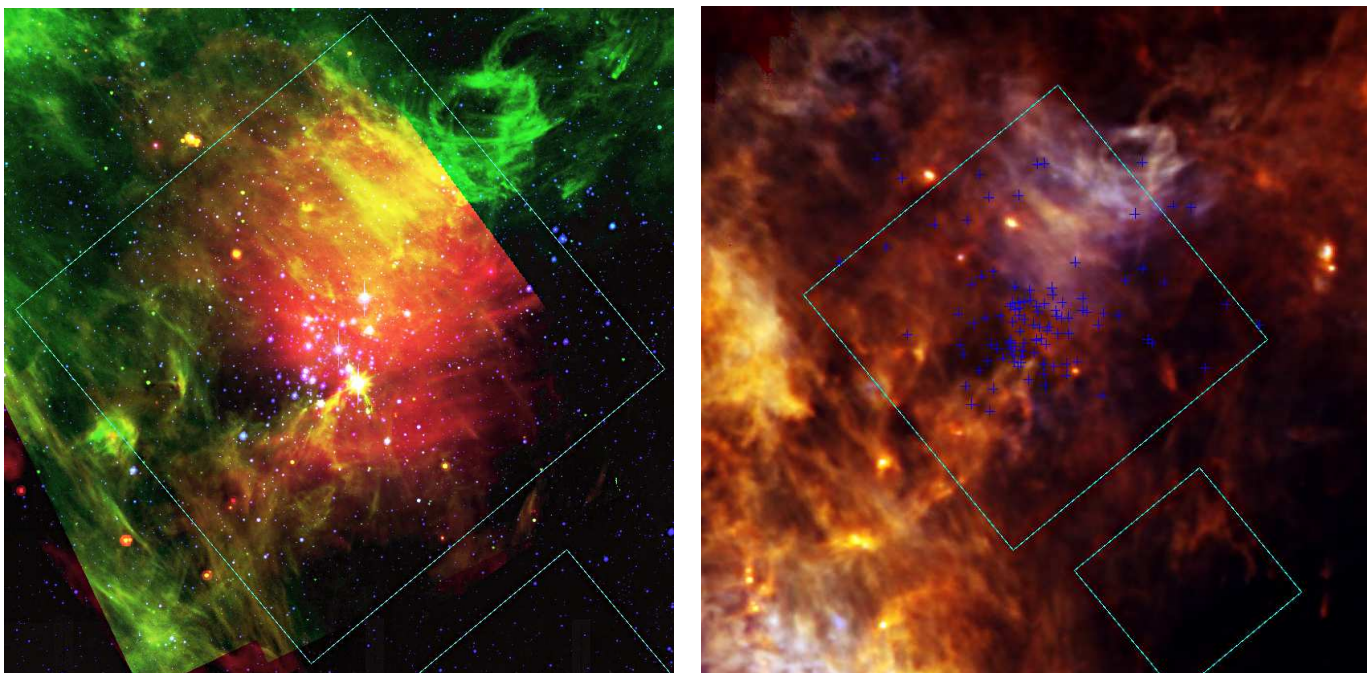


Fig. A.1. Left: Three-color composite image of the NGC 3293 area, showing the VST r -band image (from the VPHAS+ survey) in the blue color channel, the *Spitzer* IRAC $8\ \mu\text{m}$ image (retrieved from the *Spitzer* archive) in green, and the *Spitzer* MIPS $24\ \mu\text{m}$ image in red. The *Spitzer* images cover only parts of the full area shown in this image. North is up and east to the left. The cyan rectangle marks the $17' \times 17'$ area covered by our *Chandra* observation with the ACIS-I array, the lower cyan rectangle (extending beyond the edge of the image) marks the area covered by the single active ACIS-S detector.

Right: Three-color composite image showing the *Herschel* PACS $70\ \mu\text{m}$ image in the blue color channel, the PACS $160\ \mu\text{m}$ image in green, and the SPIRE $250\ \mu\text{m}$ image in red; these *Herschel* maps were obtained as part of the Hi-Gal survey and were retrieved from the archive. The B-type stars listed in Evans et al. (2005) are marked by blue crosses. The cyan rectangles mark again the *Chandra* ACIS field of view.

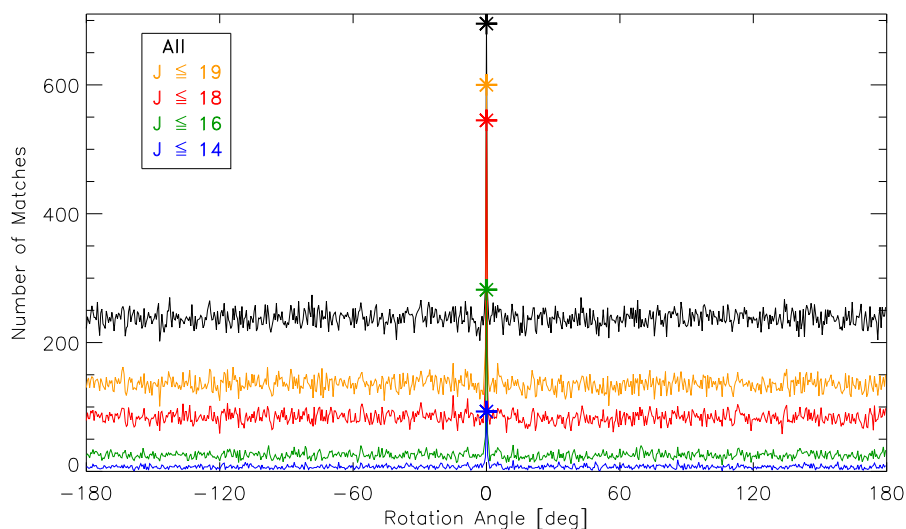


Fig. B.1. Results of the random source matching simulations. The number of VISTA catalog matches is shown as a function of the rotation angle for the X-ray source positions. The black line shows the results when using the full VISTA catalog, and the colored lines show the results when using various restricted versions of the VISTA catalog with different magnitude limits. The thick asterisks mark the number of matches found with the original (i.e., unrotated) X-ray source catalog.

are bright enough to be considered $\geq 1 M_{\odot}$ stars in NGC 3293 is quite small ($\lesssim 4\%$).

Appendix C: Random match with an artifact in the VST images

A particularly interesting case of a random false match of an X-ray source with an artifact in the VST optical catalog concerns the *Chandra* Source 407, which is located 9 arcmin south of the cluster center. The X-ray source yielded 12.8 net counts with a median photon energy of 1.9 keV.

The VST VPHAS-DR2 Point Source Catalogue lists a source VPHASDR2 J103541.2-582259.4 1735b-31-6789 with magnitudes $r = 18.1483 \pm 0.026$, $i = 17.9260 \pm 0.037$, and $H\alpha = 17.8223 \pm 0.022$, which provides a possible match to the X-ray source.

The ESO archive contains 16 individual VST observations of this point, obtained in the u , g , r , i , and the $H\alpha$ band. Our inspection of all these individual images yielded a very surprising result. While we could clearly confirm the presence of a point-like source in the u -band and g -band images obtained on 15 Feb 2012 and in the r -band, i -band, and $H\alpha$ images obtained on 30 April 2012 (see Fig. C.1), all other available VST images, which were

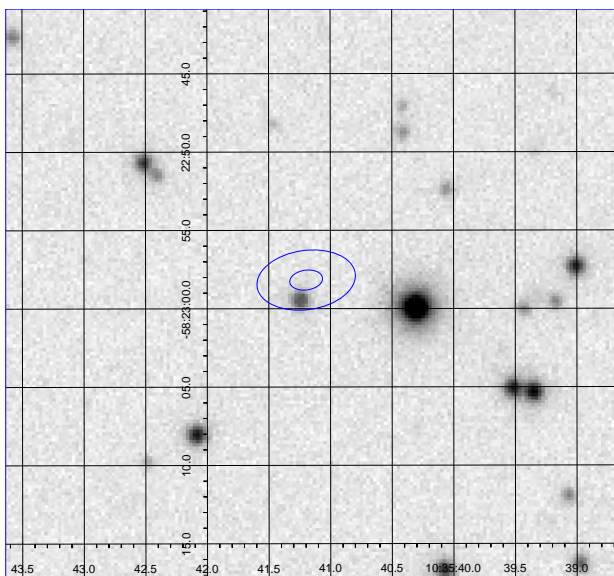


Fig. C.1. VST *i*-band image of the region around the Chandra Source J103541.19-582258.1. The small blue ellipse shows the 1σ error region for the X-ray source position; the larger blue ellipse is three times larger.

obtained on 15 Feb 2012 and 14 Feb 2013, show no source at this position. The inspection of our VISTA images (obtained on 6 March 2012 and 8 March 2012) and archival ESO WFI images obtained on 9 Feb 2012 also showed no source at this position. Upper limits for the magnitudes in these non-detection images are $u > 21.8$, $g > 22.5$, $r > 21.8$, $i > 20.8$, and $H\alpha > 20.6$.

These numbers imply that the object brightened by several magnitudes in the six days from 9 Feb 2012 to 15 Feb 2012, was invisible six days later, again bright one month later, and again invisible in the most recent images. A possible explanation of such a very unusual behavior could be that the source is some kind of a transient object.

Finally, however, our close inspection of those VST images in which the source was visible, showed that the 2D profile of the object deviates from the normal point spread function of other sources in the surrounding. After detailed consultations with VST instrument and imaging experts at the ESO headquarters, it was finally found that the apparently highly variable object is actually an image artifact, which was caused by an electronic cross-talk effect induced by a very bright, saturated star on another CCD chip in the camera (private communication from the ESO User Support Astronomer M. Petr-Gotzens and the ESO Optical detector engineering group).

Although it is very unlikely to find an optical artifact in the very small matching region around an X-ray source, this case demonstrates that these rare coincidences can sometimes happen. This highlights the importance of a careful visual inspection of the original optical/infrared images for a reliable determination of the counterparts to the X-ray sources.

Appendix D: Quasar candidate J103621.39-581520.0

As mentioned in Sect. 2.3, the brightest X-ray source (number 943) in the ACIS-I array, with 190 net counts, has no optical counterpart. It is located $\approx 4.4'$ southeast of the cluster NGC 3293. In Fig. D.1 the *Chandra* extraction region of

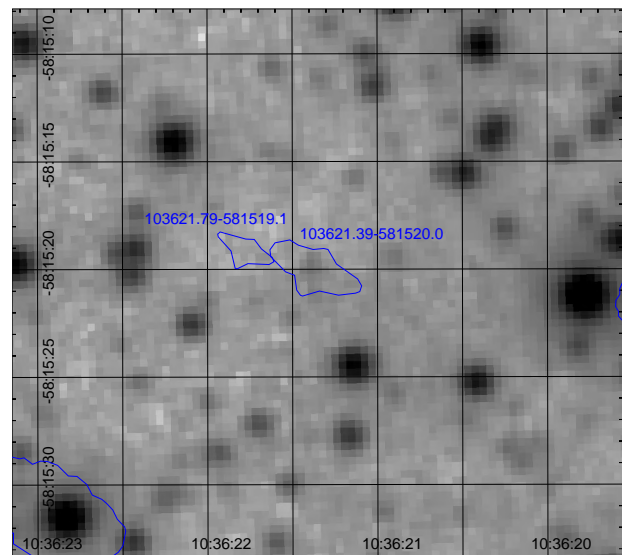


Fig. D.1. VISTA *H*-band image of the region around the quasar candidate J103621.39-581520.0. A logarithmic intensity scale was used to make the extremely faint infrared counterpart of the X-ray source J103621.39-581520.0 visible. The blue polygons show the X-ray extraction regions for the source.

J103621.39-581520.0 is shown on the VISTA *H*-band image, which reveals, at close inspection, an extremely faint infrared counterpart of this X-ray source.

The X-ray spectrum can be very nicely reproduced by a model assuming a power-law X-ray spectrum and interstellar extinction. The spectral fit yields $\chi_r^2 = 0.37$ for the following parameters: $N_H = (2.86 \pm 0.77) \times 10^{22} \text{ cm}^{-2}$ (corresponding to a visual extinction of $A_V \approx 14 \text{ mag}$), and a photo index of 1.57 ± 0.37 . The observed [0.5–8] keV X-ray flux, derived from the fit results, is $8.7 \times 10^{-14} \text{ erg cm}^{-2} \text{ s}^{-1}$, and the corresponding de-reddened X-ray flux is $1.5 \times 10^{-13} \text{ erg cm}^{-2} \text{ s}^{-1}$.

The source is invisible in all available optical VST images. From the VST *g*-band image, we estimate an upper limit of $g \geq 23 \text{ mag}$ for the brightness of the source. This corresponds to a flux of $\leq 4 \times 10^{-15} \text{ erg cm}^{-2} \text{ s}^{-1}$. Comparing this to the X-ray flux derived from the spectral fit yields an X-ray to optical flux ratio $F_X/F_{\text{opt}} \geq 21$.

These properties, i.e., the combination of strong absorption, a hard spectrum, and the very high X-ray-to-optical flux ratio, are best explained by assuming the source to be an obscured quasar. Many of these objects have X-ray-to-optical flux ratios above 1, and a small fraction of about 5% have $F_X/F_{\text{opt}} \geq 20$ (Della Ceca et al. 2015). J103621.39-581520.0 thus seems to be a particularly X-ray active quasar.

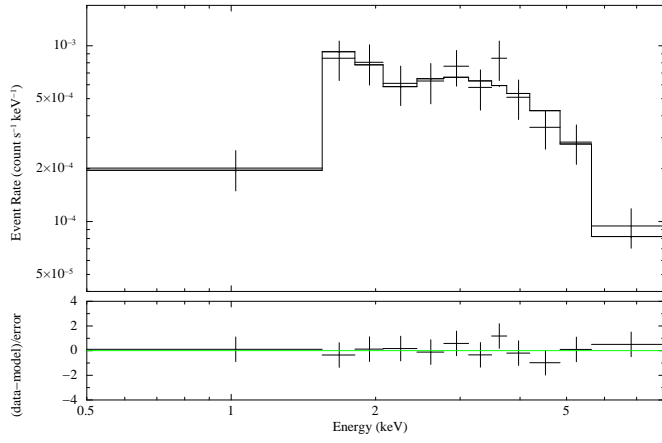


Fig. D.2. X-ray spectral fit for J103621.39-581520.0 with a power-law model.